

IFW AF



Corres. and Mail  
**BOX AF**

AMENDMENT UNDER 37 C.F.R. § 1.116  
EXPEDITED PROCEDURE  
GROUP 1774  
**PATENT APPLICATION**

**IN THE UNITED STATES PATENT AND TRADEMARK OFFICE**

In re application of

Docket No: Q68004

Kimio AKIYAMA, et al.

Appln. No.: 10/031,454

Group Art Unit: 1774

Confirmation No.: 6920

Examiner: Marie Rose Yamnitzky

Filed: January 22, 2002

For: ORGANIC ELECTROLUMINESCENT DEVICE AND LIGHT-EMITTING MATERIAL

**REQUEST FOR RECONSIDERATION UNDER 37 C.F.R. § 1.116**

**MAIL STOP AF**

Commissioner for Patents  
P.O. Box 1450  
Alexandria, VA 22313-1450

Sir:

In response to the Office Action dated May 18, 2004, reconsideration and allowance of the subject application are respectfully requested. Upon entry of this Request, Claims 1-20 are the claims pending in the application. Applicants respectfully submit that the pending claims define patentable subject matter.

Claims 1-20 were rejected under 35 U.S.C. § 112, first paragraph. The Examiner considered that defining the two organic compounds by the relationship between triplet and singlet states alone would not enable a person skilled in the art to make and use the invention in the absence of undue experimentation. Two literature references (Baldo et al. and Kobayashi et al.) were cited in support of the rejection.

**BEST AVAILABLE COPY**

Applicants traverse, and respectfully request the Examiner to reconsider in view of the following.

The present invention requires the second compound to have at least one energy level in an excited triplet state ( $T_n$ ) that lies between the energy level  $E1_{T1}$  of the first organic compound in a lowest excited triplet state and the energy level  $E2_{S1}$  of the second compound in a lowest excited singlet state, so as to enable efficient energy transfer from the first compound to the second compound.

The energy levels of the excited triplet state and singlet states can be readily determined, and the specification at pages 19-22, as well as the scientific literature available to one skilled in the art, instructs how to select combinations of compounds meeting the claimed energy levels. Relevant scientific literature (copies attached) for consideration by the Examiner include Stephen L. Murow et al., Handbook of Photochemistry 100 (Marcel Dekker, Inc. 1993), Hiroshi Fukumura et al., Temperature Effect on Inverse Intersystem Crossing Anthracenes, 42 Journal of Photochemistry and Photobiology, A: Chemistry, 283, 283-291 (1988), J.M. Larkin et al. Reverse Intersystem Crossing from a Triplet State of Rose Bengal Populated by Sequential 532- + 1064-nm Laser Excitation, Chemical Physics 244, 319-330 (1999) and Mrinalini Puranik et al., Structure of the Triplet Excited State of Bromanil from Time-Resolved Resonance Raman Spectra and Simulation, Journal of Chemical Physics, Vol. 115, No. 13, 6106-6113 (2001).

Figure 3-1 of Murow et al. at page 100 shows the absorption wavelength value  $\lambda_T$  in excitation from  $T_1$  to  $T_n$ . Electronenergy eV can be obtained by  $1240/\lambda_T$ . Fig. 3-1 also shows

the absorption wavelength value  $\lambda_s^{0-0}$  in excitation from  $S_0$  to  $S_1$  and value  $E_T^{0-0}$  in excitation from  $S_0$  to  $T_1$ .

Fukumura et al. describes anthracenes. Also, the energy levels shown in Fig. 1 at page 284 meet the requirements defined by present claim 1.

Larkin et al. teaches that the energies of rose bengal meet the requirements defined by present claim 1. *See* Table 3 at page 329

Table II at page 6110 of Puranik et al. shows singlet-triplet excitation energies of bromanil computed by TDDFT calculations. Further, Puranik et al. describes that the energy transferring from  $S_0$  to  $T_n$  is 1.62 eV. Also, the values of Puranik et al. are measured values, which confirms the accuracy of the TDDFT calculations for obtaining the precise  $T_n$  values of compounds.

One skilled in the art can readily make and/or use the invention as described in the present specification, further in view of the state of the art at the time of the invention; namely, by referring to the testing conditions described in the above publications. Although the above publications describe solution systems, as opposed to a solid system, most of the available data at the time of invention were obtained via solution systems. Furthermore, because excitation energies can be predicted by computing molecular orbital energies, as described in Puranik et al., the energy levels of a compound from one condition to another need not be taken into consideration. Thus, the energy level relationship described in Kobayashi et al. for a specific anthracene system, which is said to differ depending on the conditions under which the excited states are measured, is an exception to recognized principles rather than the rule.

In view of the above, it is respectfully submitted that the specification is fully enabling, and withdrawal of the foregoing rejection under 35 U.S.C. § 112, first paragraph, is respectfully requested.

Claims 1-20 were rejected under 35 U.S.C. § 103(a) as being unpatentable over Baldo et al. in *Nature*, Vol. 403, pp. 750-753 (February 17, 2000).

Baldo et al. was cited as teaching an electroluminescent device with a light-emitting layer comprising CBP, Ir(ppy)<sub>3</sub> and DCM2. The Examiner considered that Ir(ppy)<sub>3</sub> and DCM2 meet the energy level relationships of the claimed first and second organic compounds, respectively, and that CBP meets the limitations of the third organic compounds as recited in claims 2 and 9.

Applicants traverse, and respectfully request the Examiner to reconsider in view of the following remarks.

Baldo et al., specifically at Fig. 1 on page 751, teaches that the energy transfer from the excited triplet state of the phosphorescent sensitizer to the excited singlet state of the fluorescent dye contributes to light emission. Baldo et al. further teaches, however, that the energy transfer from a triplet state to another triplet state is a source of loss. *See* Fig. 1 Therefore, Baldo et al. does not describe a T-to-T energy transfer that contributes to light emission.

In contrast, the present invention relates to light emission by energy transfer from the excited triplet state of the first compound to the excited triplet state of the second compound, and then to the excited singlet state of the second compound. Baldo et al. does not describe such transfer or light emitting mechanism.

Although Baldo et al. discloses a relationship wherein the lowest excited triplet state of the first compound is higher than the lowest excited singlet state of the second compound by stating that the peak emission wavelength for Ir(ppy)<sub>3</sub> has a shorter wavelength and thus, a higher energy, than the peak emission wavelength for DCM2, the second compound of Baldo et al. is a compound that has a lowest excited singlet state (S<sub>1</sub>) lower than the lowest excited triplet state (T<sub>1</sub>) of the first compound.

On the other hand, the second compound of the present invention is a compound having an excited triplet state (T<sub>n</sub>) (other than the lowest excited triplet state (T<sub>1</sub>)) which is lower than the lowest excited triplet state of the first compound. This aspect of the invention would not have been obvious over Baldo et al., and there is nothing in Baldo et al. which would lead one of ordinary skill to select the claimed second organic compound. That is, the specific combination of compounds for producing an organic EL device having high efficiency according to the present invention is essentially different from that taught by Baldo et al. An organic EL device having the requisite high efficiency can be achieved only by selecting the specific combination of compounds as defined by present claim 1 and following the concepts taught in Applicants' specification.

In view of the above, it is respectfully submitted that claims 1-20 are patentable over Baldo et al., and withdraw of the foregoing rejection under 35 U.S.C. § 103(a) is respectfully requested.

Withdrawal of all of the rejections and allowance of claims 1-20 is earnestly solicited.

In view of the above, reconsideration and allowance of this application are now believed to be in order, and such actions are hereby solicited. If any points remain in issue which the Examiner feels may be best resolved through a personal or telephone interview, the Examiner is kindly requested to contact the undersigned at the telephone number listed below.

The USPTO is directed and authorized to charge all required fees, except for the Issue Fee and the Publication Fee, to Deposit Account No. 19-4880. Please also credit any overpayments to said Deposit Account.

Respectfully submitted,



Patrick F. Gallagher  
Registration No. 54,109

SUGHRUE MION, PLLC  
Telephone: (202) 293-7060  
Facsimile: (202) 293-7860

WASHINGTON OFFICE

**23373**

CUSTOMER NUMBER

Date: August 13, 2004



# Handbook of Photochemistry

Second Edition, Revised and Expanded

Steven L. Murov

*Modesto Junior College  
Modesto, California*

Ian Carmichael

*University of Notre Dame  
Notre Dame, Indiana*

Gordon L. Hug

*University of Notre Dame  
Notre Dame, Indiana*



MARCEL DEKKER, INC.

NEW YORK • BASEL

Library of Congress Cataloging-in-Publication Data

Murov, Steven L.

Handbook of photochemistry / Steven L. Murov, Ian Carmichael, Gordon L. Hug. -- 2nd ed., rev. and expanded.

p. cm.

Includes bibliographical references and index.

ISBN 0-8247-7911-8 (acid-free paper)

1. Photochemistry--Tables. I. Carmichael, Ian. II. Hug, Gordon L.

III. Title.

QD719.M87 1993

541.3'5'0212--dc20

93-4764

CIP

The publisher offers discounts on this book when ordered in bulk quantities. For more information, write to Special Sales/Professional Marketing at the address below.

This book is printed on acid-free paper.

Copyright © 1993 by MARCEL DEKKER, INC. All Rights Reserved.

Neither this book nor any part may be reproduced or transmitted in any form or by any means, electronic or mechanical, including photocopying, microfilming, and recording, or by any information storage and retrieval system, without permission in writing from the publisher.

MARCEL DEKKER, INC.

270 Madison Avenue, New York, New York 10016

Current printing (last digit):

10 9 8 7 6 5 4

PRINTED IN THE UNITED STATES OF AMERICA

## Preface

More than twenty years have passed since the publication of the first edition of this handbook. In 1972 the laser was still an infant on the photochemical scene whereas today its routine use has diminished the time scale of commonly studied transients to the picosecond range. The total number of abstracts in *Chemical Abstracts* has approximately doubled during this period and probably along with it the number of photochemical papers. This productivity coupled with the fact that the number of citations to the *Handbook of Photochemistry* in *Science Citation Index* continues to increase annually suggested that the time was ripe for a second edition. Preparation of a second edition became possible with the generous offer of support and assistance from the Radiation Chemistry Data Center at the University of Notre Dame.

The Radiation Chemistry Data Center collects and indexes current literature within its scope which now includes photochemical and photophysical processes in solution. Most of the citations used to update this book were located using the RCDC Bibliographic Database (RCDCbib). Without the availability of this database, preparation of this update would have presented an insurmountable task.

As with the first edition, the goal of this photochemical data compilation is to put at your fingertips the information needed to set up an optimal photochemical system on the first try. The types of information needed are many and varied depending on the nature of your experiment. We have attempted to devise tables organized according to the type of experiment you are likely to perform. Because of the advances in the types of equipment available such as tunable dye lasers, the already mentioned doubling of accumulated data, and the facility of referencing using RCDCbib's reference codes, a considerable reorganization of the tables was deemed appropriate.

In the first edition, the first section was divided into three parts. The first and second parts were alphabetical listings of compounds that included important photochemical parameters such as singlet and triplet energies and lifetimes. Because of frequency of use as photosensitizers and quenchers, 42 of these compounds were distinguished by inclusion in the first table along with additional parameters such as quantum yields of fluorescence, intersystem crossing, and extinction coefficients at the commonly utilized mercury emission lines. Because of the number of parameters and the basic goal of the book to include a citation for every entry, it was necessary to reference the first table in a rather unusual roadmap fashion. Because such a system would be inconvenient with the RCDCbib reference codes, a different type of table organization seemed more appropriate. The compounds of the first two tables were combined, along with a new selection of other compounds, into one table in the second edition.

Left out of this new table are the extinction coefficients of the commonly used sensitizers and quenchers. However, absorption spectra of selected sensitizers have been vastly



Table 2—Triplet State Energies—Continued

No.	Compound	$E_T(n)$			$E_T(p)$		
		kJ/mol	cm <sup>-1</sup>	Ref.	kJ/mol	cm <sup>-1</sup>	Ref.
997	Methyl methacrylate	358 <sup>g</sup>	29900 <sup>g</sup>	89M184			
998	Pyridine, 4-hydroxy-				358	29940	76E691
999	Methyl acrylate	372 <sup>g</sup>	31100 <sup>g</sup>	89M184			
1000	Pyridinium, 2-amino-				392	32800	81E297
1001	Acetylene	502 <sup>g</sup>	41900 <sup>g</sup>	78M177			
1002	1-Butyne	502 <sup>g</sup>	41900 <sup>g</sup>	78M177			

<sup>b</sup> Aromatic solvent, benzene-like; <sup>a</sup> Gas-phase measurement; <sup>x</sup> Crystalline medium

## Section 3

### Flash Photolysis: Designing Experiments

Table 3 is intended to bring together information pertinent to designing triplet-triplet energy transfer experiments in flash photolysis. These experiments are central to triplet photosensitized photochemistry, measurements of triplet quenching rates, and estimations of many triplet-triplet extinction coefficients. Table 3 can also be useful for the design of steady-state photochemistry, but triplet extinction coefficients and corresponding wavelengths are included which are needed to quickly monitor time-resolved experiments.

The information presented in Table 3 is shown pictorially in Fig. 3-1. The data for four of the columns is already presented in Table 1 in SI units, although the criteria used for the selection of compounds in Section 1 differ from that adopted here. For convenience, the triplet energy,  $E_T$ , in Table 3 is given in units of kcal/mol, and the singlet energy is given as an excitation wavelength,  $\lambda_S^0$ . The other two items from Table 1, namely the triplet quantum yields,  $\phi_T$ , and triplet lifetimes,  $\tau_T$ , are carried along unmodified.

The central new item of Table 3 is the information on triplet-triplet absorption. Whenever possible, this absorption is characterized by both a wavelength,  $\lambda_T$ , and a molar absorption coefficient,  $\epsilon_T$ , at that wavelength. When an absorption maximum exists, the wavelength refers to that maximum. In cases where molar absorption coefficients are not available, but the triplets are important donors or acceptors, only a wavelength is given, and this isolated wavelength refers to an absorption maximum. Molar absorption coefficients are often called decadic extinction coefficients. A review of the primary literature was presented previously, [86Z026] and an extensive statistical analysis of this data was also performed, [87Z100] leading to the publication of a set of recommended values for, and procedures for the determination of the molar absorptivity of transients, [91B003]

In Table 3, the solvent type is a dual one. Benzene and some aromatic solvents have a large influence on triplet-triplet absorption. There is a strong tendency to broaden the peaks such that the extinction coefficient at the maximum is lowered, but the oscillator strength (related to the total area) in the transition remains constant. To distinguish aromatic solvents for the ( $\lambda_T$ ,  $\epsilon_T$ ) pair of a given compound remains constant. "b" for "benzene-like" is used for aromatic solvents, and "nb" is used for other solvents. One or the other of these two symbols follow the "f" in the solvent column and refer only to the ( $\lambda_T$ ,  $\epsilon_T$ ) column. The symbol preceding the "f" in the solvent column is a nonpolar/polar classification (discussed in the introduction of Section 1) for the four properties,  $\lambda_S^0$ ,  $E_T$ ,  $\phi_T$ , and  $\tau_T$ .

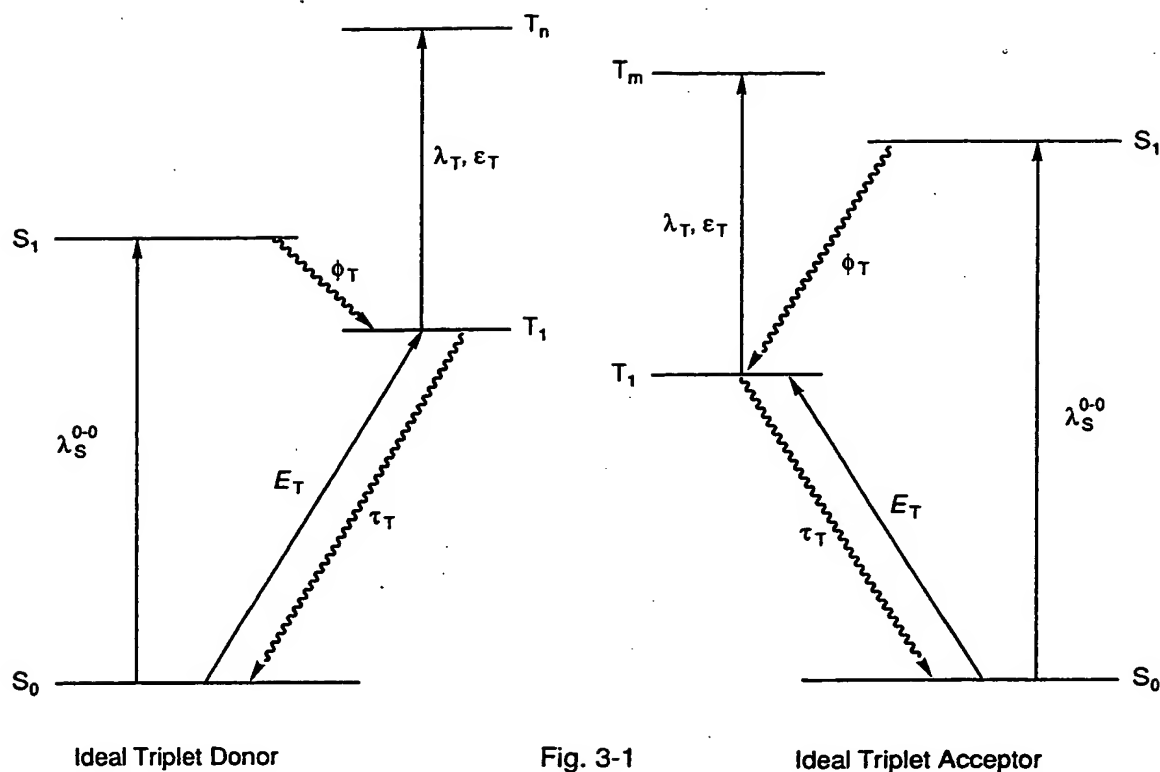


Table 3

Flash Photolysis Parameters

No.	Solv	$\lambda_S^{0-0}$ (nm)	Ref.	$E_T$ (kcal/mol)	Ref.	$\phi_T$	Ref.	$\lambda_T$ (nm), $\epsilon_T$ ( $M^{-1} cm^{-1}$ )	Ref.	$\tau_T$ ( $\mu s$ )	Ref.
<b>1 Acenaphthene</b>											
	n/b	319	71Z001	59.7	64E037	0.46	69E202	422	82A292		
	p/nb	318	68Z003	59.2	67E112	0.58	68E098	430, 6000	87Z100	3300	68Z003
<b>2 Acetone</b>											
	n					0.90	707357			6.3	84B051
	p/nb			79.4	66E095	1	66F206	300, 600	87Z100	47	717489
<b>3 Acetophenone</b>											
	n	363	64E028	74.1	81E561	1	85A268			0.23	717179
	p/nb	354	81E561	74.4	81E561	1	85A268	330, 7160	87Z100	0.14	717179
<b>4 Acetophenone, 4'-methoxy-</b>											
	n	352	66E094	71.8	67F523	1	85A268				
	p/nb			71.5	67F521	1	85A268	360, 8840	87Z100		
<b>5 Acetophenone, 4'-methyl-</b>											
	n	352	68F298	72.9	72E294	1	85A268				
	p/nb			72.8	67F521	1	85A268	331, 11400	737198		
<b>6 Acetophenone, 4'-phenyl-</b>											
	n			61.1	67F523						
	p/nb			60.8	67F523			435, 130000	87Z100		
<b>7 Acetophenone, 4'-(trifluoromethyl)-</b>											
	n	360	68F298	71.7	67F523	1	85A268				
	p/nb	360	697155	72.0	67F523	1	85A268	455, 2290	87Z100		

Table 3—Flash Photolysis Parameters—Continued

No.	Solv	$\lambda_s^{0.0}$ (nm)	Ref.	$E_T$ (kcal/mol)	Ref.	$\Phi_T$	Ref.	$\lambda_T$ (nm), $\epsilon_T$ ( $M^{-1} \text{ cm}^{-1}$ )	Ref.	$\tau_T$ ( $\mu\text{s}$ )	Ref.
23	Anthracene, 9,10-dichloro-	n/b 401	71Z001	40.5	566006	0.29	84E393	425, 46000	84E393	100	62E009
		p/nb 403	66E086	40.5	66E086	0.45	706054	425, 42500	87Z100		
24	Anthracene, 9,10-dicyano-	n/b 421	85A009	41.7	78E414	0.23	84E393	440, 9000	84E393	100	78E414
		p/nb 428	85A009					440, 9180	87Z100		
25	Anthracene, 9,10-dimethyl-	n/b 398	71Z014			0.02	68F286	435, 35300	87Z100	8000	67E129
		p/nb 403	68Z003			0.032	68Z003	435, 35300	87Z100		
26	Anthracene, 9,10-diphenyl-	n/b 393	85E096	40.9	68E131	0.02	83E281	445, 14500	87Z100	2500	746270
		p/nb 392	71Z014			0.02	83E281	445, 15600	87Z100	3000	746270
27	Anthracene, 9-methyl-	n/b 387	85E096	41.3	57B004	0.48	756505	430, 42000	690087	10000	67E129
		p/nb 391	68Z003	40.7	66E086	0.67	67E129	430, 45900	87Z100		
28	Anthracene, 9-phenyl-	n 387	71Z001			0.37	65F031			15000	67E129
		p/nb 394	68Z003			0.51	67E109	428, 14600	87Z100		
29	1-Anthracenesulfonate ion	p/nb				0.98	85E452	440, 20000	85E452	103	85E452

Section 3

30	2-Anthracenesulfonate ion	p/nb				0.65	85E452	425, 30000	85E452	83	85E452
31	9,10-Anthraquinone	n/b 421	85E712	62.4	64E021	0.90	65F030	390, 10300	720392	0.11	81F130
		p 62.8		62.8	67E115						
32	Anthrone	n								0.170	766464
		p/nb		71.9	706018			341, 74000	87Z100		
33	Azulene	n/b 704	71Z014	39	757247			360, 4000	81F275	11	84E491
		p/nb						360, 4140	87Z100	3	81F275
34	Benz[b]acridin-12-one	n		45.7	85F172						
		p/nb 488	78E878	46.1	78E878			590, 53600	87Z100		
35	Benz[a]anthracene	n/b 385	71Z014	47.2	54E002	0.79	69E208	490, 20500	71E360	100	64E015
		p/nb 390	78E761	47.2	78E761	0.79	727047	480, 28800	71E360	9400	64E026
36	Benzene	n 260	71Z014	84.3	67F523	0.25	69E202				
		p/nb 261	506002	84.3	67F523	0.15	736048	235, 11000	87Z100		

Flash Photolysis: Designing Experiments

Table 3—Flash Photolysis Parameters—Continued

No.	Solv	$\lambda_s^{0-0}$ (nm)	Ref.	$E_T$ (kcal/mol)	Ref.	$\Phi_T$	Ref.	$\lambda_T$ (nm), $\epsilon_T$ ( $M^{-1} \text{ cm}^{-1}$ )	Ref.	$\tau_T$ ( $\mu\text{s}$ )	Ref.
8	Acridine										
	n/b			45.4	81E147	0.5	78E222	440, 24300	71E360	10000	677498
	p/nb	380	779025	45.0	84E803	0.82 <sup>a</sup>	85E408	432.5, 31500	71E360	14	78E394
9	Acridine, 3,6-diamino-										
	p/nb	485	69E235	51.1	69E235			550, 9510	87Z100		
10	Acridine Orange, conjugate monoacid										
	p/nb	524	71Z014	45.7	68Z003	0.10	727073	540, 9570	87Z100	105	79E219
11	9-Acridinethione, 10-methyl-										
	n/b	633	83E230	42.6	83E230	0.95	84E342	520, 9300	84E342	2.6	84E342
	p/nb					0.90	84E342	520, 8790	87Z100	2.3	84E342
12	Acridinium, 3,6-diamino-										
	p/nb	478	71Z014	48.9	68Z003	0.22	727073	550, 8270	87Z100	20	80F373
13	Acridinium, 3,6-diamino-10-methyl-										
	p/nb	485	69E235	51.1	69E235			620, 8600	87Z100		
14	9-Acridinone										
	n/b	393	78E542	58.2	78E542	0.99	766377	620, 37800	766377	20	766377
	p/nb	413	78E542	60.2	78E878			620, 41400	87Z100	9.2	89A120
15	Angelicin										
	n					0.009	78E157				
	p/nb	362	73E372	63.2	73E372	0.031	84E794	450, 4330	87Z100	2.6	84E794
16	Aniline										
	n	300	82B140	71.0	67E116	0.75	80E253			0.72	87B098
	p/nb	312	80E253	76.6	44E001	0.90	80E253	320	69E215		
17	Aniline, <i>N,N</i> -dimethyl-										
	n	313	71Z001								
	p/nb	319	71Z001	75.8	61E013			460, 4000	85E653		
18	Aniline, <i>N</i> -phenyl-										
	n					0.32	706243			0.3	706243
	p/nb	322	73E359	71.9	73E359	0.47	706243	530, 10400	71E360	0.5	706243
19	Anthracene										
	n/b	376	85E096	42.5	57B004	0.71	757282	432.5, 45500	71E360	670	85E555
	p/nb	375	779025	42.5	779025	0.66	85E408	425, 64700	71E360	3300	747049
20	Anthracene, 9-bromo-										
	n/b	390	79E108					430, 48000	690087	43	62E009
	p/nb			41.3	84B110	0.98	89B155	430, 47500	87Z100	19.5	84B110
21	Anthracene, 9-cyano-										
	n/b	403	81E183			0.040	737140	435, 10300	690087	600	737140
	p/nb	417	737140			0.021	737140	435, 8490	87Z100	1800	737140
22	Anthracene, 9,10-dibromo-										
	n/b	406	84E393	40.2	566006	0.70	84E393	427.5, 48000	84E393	36	62E009
	p/nb	405	756125			0.82	84E785	425, 46300	87Z100	11	78E394

Table 3—Flash Photolysis Parameters—Continued

No.	Solv	$\lambda_s^{0-0}$ (nm)	Ref.	$E_T$ (kcal/mol)	Ref.	$\phi_T$	Ref.	$\lambda_T$ (nm), $\epsilon_T$ ( $M^{-1} \text{ cm}^{-1}$ )	Ref.	$\tau_T$ ( $\mu\text{s}$ )	Ref.
37	Benzene, chloro- n p/nb	272	71Z014	81.7	59E009	0.6	83F178	300, 6150	87Z100	1.6	84E529
						0.7	85E488			0.715	85E488
38	Benzene, 1,4-dichloro- n p/nb	282	82B140	80.1	67E112	0.8	83F178	310, 3800	85E406	430	85E406
		280	79B163			0.95	85E406			330	85E406
39	Benzene, methoxy- n p/nb	274	496002	80.7	67F523	0.64	82E060	252	757161	3.3	757161
		278	82B140	80.7	67F523						
40	Benzidine, $N,N,N',N'$ -tetramethyl- n p/nb			62.3	767177	0.52	84E405	475, 38700	87Z100	5	84F074
						0.41	84E405				
41	Benzil n p/nb	485	69E223	53.4	67E119	0.92	65F030	480	79E690	150	717447
				54.3	67E119					1500	68E128
42	Benzo[a]coronene n p/nb	432	59E013	51.5	78E314	0.55	68E104	570, 22300	87Z100		
43	Benzoic acid n p/nb	279	71Z014	77.5	63E014			320, 1000	87Z100		
				77.9	767546						
44	Benzo[rs]pentaphene n/b p/nb	433	64Z007	40.2	62E015			490	71E361	170	71E361
		433	779025	40.4	779025			490	71E361		
45	Benzo[ghi]perylene n/b p/nb	408	696020	46.3	566005	0.53	696020	470	71E361	150	71E361
		407	779025					465, 39300	87Z100		
46	Benzo[c]phenanthrene n p/nb	370	71Z014	56.7	54E002			517, 4800	58E001		
		373	779025	57.1	779025						
47	Benzophenone n/b p/nb	379	64E028	68.6	67F523	1.0	69E202	530, 7220	83B067	6.9	776016
		384	63Z003	69.2	80E223	1	85A268	525, 6250	87Z100	50	766276
48	Benzophenone, 4,4'-bis(dimethylamino)- n p/nb	405	79E210	65.8	68E135	0.91	777004	500	777603	25	777603
				60.8	79E210	0.47	85A268			20	777603
49	Benzophenone, 4-chloro- n p/nb			68.3	68F291	1	85A268	320, 12800	84B033		
				68.8	68F291	1	85A268				
50	Benzophenone, 4,4'-dichloro- n p/nb			68.0	64E021	1	85A268	320, 23300	87Z100	2.2	776016
				68.4	87F368	1	85A268				

Table 3—Flash Photolysis Parameters—Continued

No.	Solv	$\lambda_s^{00}$ (nm)	Ref.	$E_T$ (kcal/mol)	Ref.	$\Phi_T$	Ref.	$\lambda_T$ (nm), $\epsilon_T$ ( $M^{-1} \text{ cm}^{-1}$ )	Ref.	$\tau_T$ ( $\mu s$ )	Ref.
51	Benzophenone, 4,4'-dimethoxy-										
	n	365	66E094	70.0	81E099	1	85A268			3.6	776016
	p/nb			69.8	80E223	1	85A268	350, 14100	87Z100		
52	Benzophenone, 4-fluoro-										
	n			68.9	68F291	1	85A268				
	p/nb			69.8	81C032	1	85A268	315, 21900	87Z100		
53	Benzophenone, 4-methoxy-										
	n			68.6	68F291	1	85A268				
	p/nb			69.4	80E223	1	85A268	335, 10100	87Z100	7.2	82A082
54	Benzophenone, 4-methyl-										
	n	370	697155	68.6	67F523	1	85A268				
	p/nb	366	697155	69.4	80E223	1	85A268	315, 21100	87Z100		
55	Benzophenone, 4-(trifluoromethyl)-										
	n	373	697155	67.6	68F291	1	85A268				
	p/nb	368	697155	68.1	68F291	1	85A268	320, 22400	87Z100		
56	Benzo[g]pteridine-2,4-dione, 7,8,10-trimethyl-										
	n									30	68E100
	p/nb	500	69E235	50.0	69E235	0.30	777617	650, 6090	87Z100	320	70E295
57	Benzo[a]pyrene										
	n/b	405	71Z014	41.9	57B004			475	71E361	8700	78A345
	p/nb	403	779025	42.3	779025			465	78A345	8800	64E026
58	Benzo[e]pyrene										
	n/b	368	71Z014					560	71E361	120	71E361
	p/nb	366	779025	52.8	779025			555, 17000	87Z100		
59	1,4-Benzoquinone										
	n	457	69E247	53.6	69E247						
	p/nb							450	79B007	0.53	80B112
60	1,4-Benzoquinone, tetrachloro-										
	n/b	450	69E247	49.2	69E247			516	727069	2.0	697272
	p/nb					0.98	79B061	510, 6990	87Z100	1.2	697272
61	1,4-Benzoquinone, tetramethyl-										
	n/b					1.0	767144	490, 6950	71E360	21	767144
	p/nb					1.0	767144	490, 5330	71E360	15	767144
62	Benzo[b]triphenylene										
	n/b	375	71Z014	50.9	57B004			450	71E361	90	71E361
	p/nb	374	779025	50.9	779025			450, 29900	87Z100		
63	Benzoxazole, 2,2'-(1,4-phenylene)bis-										
	n									0.48	82E632
	p/nb							480, 18600	87Z100		
64	Biacetyl										
	n/b					1.0	60E012	315, 5160	71E360	638	726211
	p/nb							315, 4580	87Z100		

Section 3

Flash Photolysis: Designing Experiments

Table 3—Flash Photolysis Parameters—Continued

No.	Solv	$\lambda_s^{0-0}$ (nm)	Ref.	$E_T$ (kcal/mol)	Ref.	$\phi_T$	Ref.	$\lambda_T$ (nm), $\epsilon_T$ ( $M^{-1} \text{ cm}^{-1}$ )	Ref.	$\tau_T$ ( $\mu s$ )	Ref.
65	1,1'-Binaphthyl										
	n	325	71Z001							14	771048
	p/nb	328	776226					615, 12400	87Z100		
66	2,2'-Binaphthyl										
	n	333	71Z001								
	p/nb			55.9	566005			450, 24800	87Z100		
67	Biphenyl										
	n/b	286	71Z001	65.4	64E037	0.84	757282	367.3, 27100	71E360	130	69E208
	p/nb	306	776226	65.5	735067			361.3, 42800	71E360		
68	Biphenyl, 4,4'-diamino-										
	p/nb	346	71Z001					460, 35500	87Z100		
69	Biphenylene										
	n	392	64Z007							100	720464
	p/nb							350, 10500	87Z100		
70	1,3-Butadiene, 1,4-diphenyl-										
	n/b			42.3	707199	0.020	82E365	390, 45000	87Z100	1.6	82E365
	p/nb	358	80B135			$\leq 0.002$	82E365	390, 54500	87Z100	5.0	84E319
71	C <sub>60</sub>										
	n/b	620	91E003	36.0	91E368	1	92E260	740, 12000	92E205	250	92E205
	p/nb							740, 14000	92E260		

72	C <sub>70</sub>										
	n/b	648	91E594	35.3	91D034	0.97	92E142	490, 12000	92E205	250	92E205
	p/nb							470, 19000	92E260		
73	Carbazole										
	n/b	332	71Z001			0.36	65F030	418	84F248	170	77A178
	p/nb	345	78E761	70.2	58E005			425, 14000	87Z100		
74	2,2'-Carbocyanine, 1,1'-diethyl-										
	p/nb					0.0029	79E243	635, 58000	87Z100	190	79E243
75	4,4'-Carbocyanine, 1,1'-diethyl-										
	p/nb					$< 6 \times 10^{-4}$	736051	778, 35600	87Z100	1100	736051
76	$\beta$ -apo-8'-Carotenal										
	n	518	78E431			0.003	78E721			10	733001
	p/nb							520, 223000	87Z100		
77	$\beta$ -apo-14'-Carotenal										
	n/b	457	78E432			0.54	79E546	480, 114000	87Z100	8	83E026
	p/nb	465	78E432			-0.033	79E546	480, 116000	87Z100	10.3	79E546
78	$\beta$ -Carotene										
	n/b	524	71Z014	21	757247	$< 0.001$	776412	520	767094	70	66E089
	p/nb	704	92N199	20.3	92N199			515, 187000	87Z100	9	81B115
79	Chlorophyll <i>a</i>										
	n/b	677	81F121					460	55E003	1500	58R001

Table 3—Flash Photolysis Parameters—Continued

No.	Solv	$\lambda_s^{0.0}$ (nm)	Ref.	$E_T$ (kcal/mol)	Ref.	$\phi_T$	Ref.	$\lambda_T$ (nm), $\epsilon_T$ (M <sup>-1</sup> cm <sup>-1</sup> )	Ref.	$\tau_T$ ( $\mu$ s)	Ref.
79	Chlorophyll <i>a</i> —Continued										
	p/nb	671	79E838	29.8	79E838	0.53	86R013	460, 48000	79B037	800	68Z003
80	Chlorophyll <i>b</i>										
	n/b	660	79E838	31.1	79E838			316, 36500	59B002	2500	59B002
	p/nb	667	68Z003	32.6	68Z003	0.81	86R013	450, 24300	87Z100	1500	68Z003
81	Chrysene										
	n/b	361	71Z014			0.85	757282	575	761024	710	69E208
	p/nb	360	779025	57.1	779025	0.85	68E098	580, 29800	87Z100		
82	Coronene										
	n/b	428	64Z007					480	761024		
	p/nb	429	779025	54.4	566005	0.56	68E098	480, 15000	87Z100		
83	Coumarin										
	n/b			61.7	775025			400, 11000	79E282	3.8	79E282
	p/nb	341	73E372	62.4	73E372	0.054	79E282	400, 10100	87Z100	1.3	79E282
84	Coumarin, 5,7-dimethoxy-										
	n									10	79E282
	p/nb	352	73E372	60.6	73E372	0.072	79E282	450, 10500	87Z100		
85	1,3-Cyclohexadiene										
	n/b	292	399001	52.4	65E036			310	84A458	30	80B021
	p/nb							303, 2300	87Z100		

86	Deoxythymidine 5'-monophosphate										
	p/nb	293	673066	75.2	673066	0.055	79B087	370, 4000	79B087	25	79B087
87	Dibenz[ <i>a,h</i> ]anthracene										
	n/b	395	71Z014			0.90	727047	584, 13000	83F075		
	p/nb	395	779025	52.1	779025	0.9	83F075	580, 25100	87Z100		
88	2,2'-Dicarbocyanine, 1,1'-diethyl-										
	p/nb					$<3 \times 10^{-4}$	736051	780, 69300	87Z100	480	736051
89	Fluorene										
	n	301	71Z014	67.5	64E037	0.22	706049			150	69E208
	p/nb	301	779025	67.9	779025	0.32	68E098	380, 22700	87Z100		
90	9-Fluorenone										
	n/b					0.94	757282	430, 5900	757282	500	78E495
	p/nb	450	706018	50.3	78E060	0.48	78E495	425, 6040	87Z100	100	78E495
91	Fluorescein dianion										
	p/nb	520	69E235	47.2	69E235	0.02	82E660	535, 8700	60A001	20000	60A001
92	Fluorescein dianion, 2',4',5',7'-tetrabromo-										
	p/nb	571	68Z004	42.3	68Z004	0.33	82E660	580, 10200	87Z100	30	84E216
93	Fluorescein dianion, 2',4',5',7'-tetraiodo-										
	p/nb	565	68Z004	44.0	69E203	0.83	82E660	526, 26000	67E031	630	64E016
94	( <i>E,E,E</i> )-2,4,6-Heptatrienal, 5-methyl-7-(2,6,6-trimethyl-1-cyclohexen-1-yl)-										
	n/b	400	78E431	35.9	84E180	0.66	79E546	430, 63000	79E546	6.2	79E546



Table 3—Flash Photolysis Parameters—Continued

No.	Solv	$\lambda_s^{0-0}$ (nm)	Ref.	$E_T$ (kcal/mol)	Ref.	$\phi_T$	Ref.	$\lambda_T$ (nm), $\epsilon_T$ ( $M^{-1} \text{ cm}^{-1}$ )	Ref.	$\tau_T$ ( $\mu\text{s}$ )	Ref.
94	(E,E,E)-2,4,6-Heptatrienal, 5-methyl-7-(2,6,6-trimethyl-1-cyclohexen-1-yl)—Continued										
	p/nb					0.41	79E546	440, 52000	87Z100	10.9	79E546
95	1,3,5-Hexatriene, 1,6-diphenyl-			35.6	72B007	0.029	82E365	420, 105000	87Z100	20	82E365
	n/b										
	p/nb	399	78B145			0.020	761088	420, 114000	87Z100	30	82E365
96	Indole										
	n/b	288	51Z002	72.0	84E843	0.43	81E082	430	771021	16	777037
	p/nb	299	63E012	70.8	84E843	0.23	81E082	430, 4260	87Z100	11.6	757163
97	$\beta$ -Ionone										
	n/b	405	85E293	55	85E293	0.49	85E293	345	85E293	0.16	78E721
	p/nb							330, 85300	87Z100		
98	Isoquinoline										
	n			60.6	59E009	0.21	87E642				
	p/nb	320	59E008	60.6	59E008			418, 11900	87Z100		
99	Methylene Blue cation										
	p/nb	664	63E027	33	67F524	0.52	69E203	420, 14400	87Z100	450	756162
100	Naphthalene										
	n/b	311	71Z014	60.6	57B004	0.75	757282	425, 13200	71E360	175	62E009
	p/nb	311	506002	60.9	44E001	0.80	68E098	415, 24500	71E360	1800	747049
101	Naphthalene, 1-bromo-										
	n	321	71Z014	59.0	57B004					270	62E009

Section 3

101	Naphthalene, 1-bromo—Continued										
	p/nb			59.0	63Z003			425, 11500	87Z100	830	61E005
102	Naphthalene, 1-chloro-										
	n			58.6	78E067	0.79	757282			280	62E009
	p/nb	319	79B163	59.2	44E001			420, 29500	87Z100		
103	Naphthalene, 1,4-dicyano-										
	n	336	84F449								
	p/nb			55.5	767370	0.19	84B066	455, 6730	87Z100	40	84B066
104	Naphthalene, 1,4-diphenyl-										
	n	336	71Z001								
	p/nb							444, 32500	87Z100		
105	Naphthalene, 1-hydroxy-										
	n	321	71Z001			>0.27	65F030				
	p/nb	323	71Z014	58.6	44E001			430, 9000	85A406		
106	Naphthalene, 2-hydroxy-										
	n	330	71Z001							67	737113
	p/nb	330	71Z014	60.3	44E001			435, 6680	87Z100		
107	Naphthalene, 1-methoxy-										
	n					0.45	757282				
	p/nb	320	79B163	59.8	44E001	0.50	68E098	440, 9980	87Z100	5500	68Z003

Flash Photolysis: Designing Experiments

Table 3—Flash Photolysis Parameters—Continued

No.	Solv	$\lambda_s^{0-0}$ (nm)	Ref.	$E_T$ (kcal/mol)	Ref.	$\phi_T$	Ref.	$\lambda_T$ (nm), $\epsilon_T$ ( $M^{-1} \text{ cm}^{-1}$ )	Ref.	$\tau_T$ ( $\mu\text{s}$ )	Ref.
108	Naphthalene, 2-methoxy-					0.50	757282			50	77E663
	n							435, 21400	87Z100		
	p/nb										
109	Naphthalene, 1-methyl-					0.58	757282	425	84E092	25	767159
	n/b	317	71Z001	60.6	44E001			420, 20200	87Z100		
	p/nb	317	71Z014								
110	Naphthalene, 2-methyl-					0.56	757282				
	n	319	71Z001	60.8	67E112			420, 30600	87Z100		
	p/nb	319	71Z014								
111	Naphthalene, 1-nitro-					0.63	687061			0.93	81B064
	n	382	71Z014	55.2	71F587			525	81B064	4.9	81B064
	p/nb										
112	Naphthalene, 2-nitro-					0.83	71F587			0.53	767269
	n	380	71Z014	56.9	71F587			360, 3600	87Z100	1.70	767269
	p/nb										
113	Naphthalene, 1-phenyl-					0.52	757282				
	n	315	71Z001	58.8	67E112			490, 21700	87Z100		
	p/nb										
114	Naphthalene, 2-phenyl-					0.43	757282				
	n	325	71Z001	58.7	67E112			430, 43000	87Z100		
	p/nb										
115	1,3,5,7-Octatetraene, 1,8-diphenyl-					0.005	82E365	440, 178000	87Z100	40	82E365
	n/b	443	72E330	31.6	72B007	0.006	761088	440, 198000	87Z100	34	82E365
	p/nb										
116	1,3,4-Oxadiazole, 2,5-diphenyl-									0.300	777265
	n	311	71Z001								
	p/nb	310	71Z001					425, 980	87Z100		
117	2,2'-Oxadibocyanine, 3,3'-diethyl-					<0.005	726156	650, 81400	87Z100	5000	726156
	p/nb										
118	Oxazole, 2,5-bis(4-biphenyl)-									0.285	777265
	n	375	71Z001								
	p/nb							560, 110000	87Z100		
119	Oxazole, 2,5-diphenyl-					0.12	80E439			1700	80E439
	n	335	71Z001					500, 14800	87Z100	2500	747049
	p/nb	336	71Z001								
120	Oxazole, 2,2'-(1,4-phenylene)bis[5-phenyl-					0.054	86E128	550, 37600	86E128	1750	86E128
	n/b	379	71Z001	55.5	86E128						
	p	385	71Z001								
121	Pentacene					0.16	727073				
	n/b	585	71Z014	18.0	716279			505, 120000	727348	110	61E005
	p/nb							305, 595000	87Z100		

Table 3—Flash Photolysis Parameters—Continued

No.	Solv	$\lambda_s^{0-0}$ (nm)	Ref.	$E_T$ (kcal/mol)	Ref.	$\Phi_T$	Ref.	$\lambda_T$ (nm), $\epsilon_T$ ( $M^{-1} \text{ cm}^{-1}$ )	Ref.	$\tau_T$ ( $\mu\text{s}$ )	Ref.
122	<b>(<i>E,E</i>)-2,4-Pentadienal, 3-methyl-5-(2,6,6-trimethyl-1-cyclohexen-1-yl)-</b>										
	n	358	78E431	45.0	78E721	0.20	84E036			0.1	78E721
	p/nb					0.45	79E546	385, 32300	87Z100	0.19	79E546
123	<b>Pentaphene</b>										
	p/nb	424	64Z006	48.4	566005			493, 45900	84E390		
124	<b>Perylene</b>										
	n/b	435	71Z014	35.4	69E238	0.014	66E101	490, 14300	71E360		
	p/nb	439	68Z003	36.0	68Z003	0.0088	66E101	485, 13400	87Z100	5000	68Z003
125	<b>Phenanthrene</b>										
	n/b	346	71Z014	62.3	63E024	0.73	757282	492.5, 15700	71E360	145	62E009
	p/nb	347	79E505	61.4	89E090	0.85	68E098	482.5, 25200	71E360	910	61E005
126	<b>1,10-Phenanthroline</b>										
	n/b	342	83E180					440	82A259	26	777201
	p/nb	339	63E018	63.2	63E018			445	777201	35	777201
127	<b>Phenazine</b>										
	n/b			44.5	69E229	0.21	716169	440	717154	42	716169
	p/nb	438	79E967	44.6	85B074	0.45	85B074	355, 37700	87Z100	770	85B074
128	<b>Phenazinium, 3,7-diamino-2,8-dimethyl-5-phenyl-</b>										
	p/nb					0.50	82E660	420, 10000	87Z100	67	677322
129	<b>Phenazinium, 3,7-diamino-5-phenyl-</b>										
	p/nb					0.10	89A343	440, 29000	89A343	25	89A343
130	<b>Phenol</b>										
	n	278	71Z014			0.32	82E060				
	p/nb	283	84E090	81.7	84E090			250	757161	3.3	757161
131	<b>Phenothiazine</b>										
	n			60.4	757279						
	p/nb	370	71Z014			0.54	83E835	460, 27000	87Z100		
132	<b>Phenoxazine</b>										
	n/b	362	72E303	62.6	72E303			465	707186	32	72E303
	p/nb	366	72E303	62.2	72E303			465	707186	44	707186
133	<b>Phenoxazinium, 3,7-diamino-, conjugate monoacid</b>										
	p/nb					$\leq 0.003$	767661	650, 16000	767246	55	767246
134	<b><i>p</i>-Phenylenediamine, <i>N,N,N',N'</i>-tetramethyl-</b>										
	n/b	358	71Z001					620, 12200	87Z100	1.4	82E474
	p/nb	364	71Z001					605, 12200	71E360	0.5	84B061
135	<b>Pheophytin <i>a</i></b>										
	n	670	79E838	31.0	79E838						
	p/nb	667	70E296			0.95	70E296	407, 62800	87Z100	750	70E296
136	<b>Pheophytin <i>b</i></b>										
	n	658	79E838	32.1	79E838						
	p/nb	654	70E296			0.75	70E296	423, 71200	87Z100	1050	70E296

Table 3—Flash Photolysis Parameters—Continued

No.	Solv	$\lambda_s^{0-0}$ (nm)	Ref.	$E_T$ (kcal/mol)	Ref.	$\phi_T$	Ref.	$\lambda_T$ (nm), $\epsilon_T$ ( $M^{-1} cm^{-1}$ )	Ref.	$\tau_T$ ( $\mu s$ )	Ref.
137	Phthalazine										
	n/b			63.1	82E585	0.29	82E203	396	747093	2.7	87E642
	p/nb	387	59E008	65.8	59E008	0.44	87E642	421, 4450	87Z100	21.3	757309
138	Phthalocyanine										
	n	704	69E231	28.7	78A378	0.14	78A378			130	78A378
	p/nb							480, 29900	87Z100		
139	Phthalocyanine, magnesium(II)										
	n	687	69E231							100	65A001
	p/nb					0.23	70E319	480, 32300	87Z100	430	86E784
140	Phthalocyanine, zinc(II)										
	n/b	683	71E386	26.2	71E386	0.65	81E457	480, 51000	87Z100		
	p/nb					0.04	86E784	480, 28900	87Z100	270	86E784
141	Picene										
	n/b	376	64Z006					560	71E361	160	71E361
	p/nb	376	779025	57.4	779025			630, 45500	87Z100		
142	Porphine										
	n	615	753056	36.0	753056	0.90	82F161				
	p/nb	610	743135	36.4	743135			419, 98600	87Z100		
143	Porphine, 2,7,12,17-tetraethyl-3,8,13,18-tetramethyl-, zinc(II)										
	n	573	69E231								
	p/nb	576	71E357	40.6	71E357			440, 99000	87Z100		
144	Porphine, tetrakis(4-sulfonatophenyl)-										
	p/nb					0.78	82E622	790, 3400	84E203	420	82E622
145	Porphine, tetrakis(4-sulfonatophenyl)-, zinc(II)										
	p/nb					0.84	82E622	840, 6000	84E203	80	82N068
146	Porphine, tetrakis(4-trimethylammoniophenyl)-										
	p/nb					0.80	83E462	800, 3200	83E462	540	83E462
147	Porphine, tetrakis(4-trimethylammoniophenyl)-, zinc(II)										
	p/nb					0.82	83E462	840, 5000	83E462	1200	83E462
148	Porphine, tetraphenyl-										
	n/b	667	82Z053	33.0	82Z053	0.82	82F161	790, 6000	84E203	1500	84E203
	p/nb	645	743135	33.5	743135	0.88	83F182	785, 6000	87Z100		
149	Porphine, tetraphenyl-, magnesium(II)										
	n	611	82Z053	34.1	82Z053					1400	81E271
	p/nb	620	71E357	34.2	71E357	0.85	83F182	485, 72000	87Z100		
150	Porphine, tetraphenyl-, zinc(II)										
	n/b	605	82Z053	36.6	756229	0.88	82F161	845, 8200	84E203	1200	81E271
	p/nb	602	71E357	36.6	71E357	0.90	83F182	470, 71000	81E271		
151	Porphine, zinc(II)										
	p/nb	569	71E357	39.6	71E357			840, 7000	80N087		
152	Porphine-2,18-dipropionic acid, 7,12-diethenyl-3,8,13,17-tetramethyl-, dimethyl ester										
	n/b					0.80	82F161	710, 9000	771078	550	80B017

Table 3—Flash Photolysis Parameters—Continued

No.	Solv	$\lambda_s^{0-0}$ (nm)	Ref.	$E_T$ (kcal/mol)	Ref.	$\phi_T$	Ref.	$\lambda_T$ (nm), $\epsilon_T$ ( $M^{-1} \text{ cm}^{-1}$ )	Ref.	$\tau_T$ ( $\mu\text{s}$ )	Ref.
152	Porphine-2,18-dipropionic acid, 7,12-diethenyl-3,8,13,17-tetramethyl-, dimethyl ester—Continued										
	p	627	743135	36.0	743135						
153	Porphine-2,18-dipropionic acid, 3,7,12,17-tetramethyl-, dimethyl ester					0.63	80E200			210	80E200
	n										
	p/nb							440, 23900	87Z100		
154	Porphycene					0.42	86E633	380, 66000	86E633	200	86E633
	n/b										
155	Psoralen					0.034	78E157	450, 8100	78E157		
	n/b					0.06	79E678	450, 11200	87Z100	5	79E678
	p/nb	365	73E372	62.7	73E372						
156	Psoralen, 5-methoxy-					0.067	78E157	450, 10200	78E157		
	n/b					0.1	83E324	450, 9450	87Z100	4.2	83E324
	p/nb	375	73E372	60.7	83E324						
157	Psoralen, 8-methoxy-					0.011	78E157	480, 10000	78E157	1.1	78E157
	n/b					0.04	83E324	370, 17700	87Z100	10	79E678
	p/nb	387	73E372	62.6	73E372						
158	Psoralen, 4,5',8-trimethyl-					0.093	79B042	470, 25700	87Z100	7.1	79B042
	p/nb	372	73E372	64.0	73E372						
159	Purine										
	n			75.6	755396						
	p/nb	286	71Z014					390, 4100	87Z100		
160	Pyranthrene					0.55	83F075				
	n					0.52	83F075	500, 20600	87Z100		
	p/nb										
161	Pyrazine					0.33	67E117				
	n	327	83E031	75.4	78E312	0.87	757309	260, 3600	87Z100	4.5	757309
	p/nb			74.3	58E006						
162	Pyrene					0.37	82E042	420, 20900	71E360	180	70E295
	n/b	372	71Z014	48.4	57B004	0.38	68E098	412.5, 30400	71E360	11000	68Z003
	p/nb	373	78E761	48.2	78E761						
163	1-Pyrenecarboxaldehyde					0.78	83E387	440, 20100	83E387	50	83E387
	n/b			43	83E387	0.65	83E387	440, 18400	87Z100	38	83E387
	p/nb										
164	Quinoline					0.31	65F030				
	n	313	80E627	61.7	80E627						
	p/nb	314	80E627	62.5	83E417			425, 6750	87Z100		
165	Quinoxaline					0.99	82E203				
	n	381	82E355	61.0	82E355	0.90	85E408	425, 8100	707240	29.4	757309
	p/nb	375	59E008	60.8	59E008						
166	(all-E)-Retinal					0.43 <sup>w</sup>	75E529	450, 58400	87Z100	9.3	82A288
	n/b	426	717003	29.4	84E180	0.12 <sup>w</sup>	78E467	450, 69300	87Z100	18	62E007
	p/nb										

Table 3—Flash Photolysis Parameters—Continued

No.	Solv	$\lambda_s^{0.0}$ (nm)	Ref.	$E_T$ (kcal/mol)	Ref.	$\phi_T$	Ref.	$\lambda_T$ (nm), $\epsilon_T$ ( $M^{-1} \text{ cm}^{-1}$ )	Ref.	$\tau_T$ ( $\mu\text{s}$ )	Ref.
167	( <i>all-E</i> )-Retinol										
	n	373	69E251	33.5	84E180	0.017	776412			25	716113
	p/nb	366	69E251			~0.003	85E190	405, 80000	776412		
168	Rhodamine, inner salt, <i>N,N'</i> -diethyl										
	p/nb	534	77E801	43.9	77E801	0.005	777041	615, 12000	78A304		
169	Rhodamine 6G cation										
	p/nb	546	77E801	43.2	77E801	0.0021	747050	620, 16000	87Z100	3500	747050
170	Riboflavine, conjugate monoacid										
	p/nb	455	71Z014			0.40	777617	415, 7560	87Z100	19	777617
171	Rubrene										
	n/b	542	81E716	26.3	81E346	0.0092	86E782	495, 26000	81E716	120	86E782
	p/nb					0.023	89B155	495, 26500	87Z100	80	68E103
172	( <i>E</i> )-Stilbene										
	n/b	334	62E012	49.3	80E113			360	720447	14	680379
	p/nb			49.3	80E113			378, 34000	87Z100	62	81E214
173	Styrene										
	n	288	776060	61.8	776060	0.40	82E181			0.025	82E181
	p/nb							325, 2210	87Z100		
174	<i>p</i> -Terphenyl										
	n/b	310	71Z001			0.11	69E208	460, 90000	71E360	450	69E208
	p/nb			58.3	67E112			460, 72700	87Z100		
175	Tetracene										
	n/b	472	71Z014	29.3	64E038	0.62	757282	465, 31200	71E360	400	85E555
	p/nb	471	779025			0.66	717459	465, 57900	87Z100		
176	Thiobenzophenone										
	n/b	627	756061	39.3	756061	1.0 <sup>w</sup>	84A221	400, 4800	84A221	1.7	84A221
	p/nb	626	726174	40.6	726174			400, 4950	87Z100		
177	Thiobenzophenone, 4,4'-bis(dimethylamino)-										
	n/b	583	726174	42.2	726174	1.0	84A221	335, 14400	84A221	1.3	84A221
	p/nb							335, 14900	87Z100		
178	Thiobenzophenone, 4,4'-dimethoxy-										
	n			41.2	726174	1.0 <sup>w</sup>	84A221			1.4	84A221
	p/nb	606	726174	42.1	726174			295, 20500	87Z100		
179	Thionine cation										
	p/nb	612	697141	39	697141	0.62	69E203	770, 10900	87Z100	72	697141
180	Thionine cation, conjugate monoacid										
	p/nb							650, 18000	87Z100	16	777315
181	Thioxanthene-9-one										
	n/b			63.3	86E676			650, 30000	79E099	95	81A294
	p/nb							650, 26200	87Z100	73	737190
182	Thioxanthione										
	n/b			39.6	82E214	1.0 <sup>w</sup>	84A221	505, 2500	84A221	0.83	84A221

Table 3—Flash Photolysis Parameters—Continued

No.	Solv	$\lambda_s^{0.0}$ (nm)	Ref.	$E_T$ (kcal/mol)	Ref.	$\phi_T$	Ref.	$\lambda_T$ (nm), $\epsilon_T$ ( $M^{-1} \text{ cm}^{-1}$ )	Ref.	$\tau_T$ ( $\mu\text{s}$ )	Ref.
182	Thioxanthione—Continued										
	p/nb							505, 2580	87Z100		
183	Thymidine										
	n	284	80E025								
	p/nb	287	80E025			0.069	79B087	370, 2320	87Z100	25	79B087
184	Thymine										
	n	283	80E025								
	p/nb	283	80E025			0.06	757510	340, 4000	757510	10	757510
185	1,3,5-Triazine										
	n	327	71Z014								
	p/nb			75.5	61E009			245, 6000	87Z100	0.91	757066
186	Triphenylene										
	n/b	343	71Z001			0.86	69E202	430, 6190	87Z100	55	61E005
	p/nb	340	779025	67.0	84E612	0.89	66E098	430, 13500	87Z100	1000	61E005
187	Tryptophan										
	p/nb	300	62Z002			0.18	777432	460, 5000	87Z100	14.3	757163
188	Uracil										
	n	278	80E025								
	p/nb	278	80E025			0.1	79B087	350, 1730	87Z100	2	757510
189	Uracil, 1,3-dimethyl-										
	n	283	80E025								

Section 3

189	Uracil, 1,3-dimethyl—Continued										
	p/nb	283	80E025			0.02	81E042	380, 8000	87Z100		
190	Uridine										
	p/nb					0.078	79B087	370, 4130	87Z100	20	79B087
191	Uridine 5'-monophosphate										
	p/nb	287	673066	78.3	737541	0.044	79B087	390, 5810	87Z100	33	79B087
192	9-Xanthione										
	n/b	621	81F218	43.3	81F218	0.8 <sup>w</sup>	84A221	345, 15400	84A221	1.8	84A221
	p/nb							345, 15900	87Z100		
193	Xanthone										
	n/b	370	717449	74.1	717449			610, 5300	767171	0.02	767171
	p/nb			74.1	717449			605, 6480	87Z100	17.9	767171

<sup>s</sup> Very solvent-dependent; <sup>w</sup> Wavelength dependent

Flash Photolysis: Designing Experiments

TEMPERATURE EFFECT ON INVERSE INTERSYSTEM CROSSING  
OF ANTHRACENES

HIROSHI FUKUMURA<sup>†</sup>, KOICHI KIKUCHI, KAZUhide KOIKE and HIROSHI  
KOKUBUN<sup>‡</sup>

Department of Chemistry, Faculty of Science, Tohoku University, Aoba, Aramaki,  
Sendai 980 (Japan)

(Received September 28, 1987)

### Summary

The temperature and heavy-atom effects on the quantum yield  $\Phi_{TS}$  of the inverse ( $T_n \rightarrow S_1$ ) intersystem crossing of several anthracenes are studied by the stepwise two-photon excitation technique. The first effect is explained in terms of the relative positions of the  $S_1$  and  $T_2$  levels and the second effect in terms of the spin-orbit coupling between  $S_1$  and  $T_2$ . It was confirmed that the  $T_n \rightarrow S_1$  inverse intersystem crossing occurs from  $T_2$  to  $S_1$  after rapid  $T_n \rightarrow T_2$  internal conversion.

### 1. Introduction

Non-radiative relaxation processes from a higher excited triplet state ( $T_n$ ,  $n \geq 2$ ) have been studied using a stepwise two-photon excitation technique devised in this laboratory [1]. The variation in the quantum yield  $\Phi_{TS}$  of inverse ( $T_n \rightarrow S_1$ ) intersystem crossing for *meso*-substituted anthracenes has been interpreted in terms of spin-orbit coupling [2]. The exceptionally low value of  $\Phi_{TS}$  for anthracene was considered to be due to the fact that the energy level of  $T_2$  is lower than that of  $S_1$  for anthracene and vice versa for its *meso* derivatives; in other words, the inverse intersystem crossing occurs from  $T_2$  to  $S_1$  after  $T_n \rightarrow T_2$  internal conversion, and thermal activation is necessary for the  $T_2 \rightarrow S_1$  inverse intersystem crossing of anthracene [1, 2]. This concept has been supported by the facts that  $\Phi_{TS}$  for anthracene increases with increasing temperature whereas  $\Phi_{TS}$  for 9-methylanthracene does not depend on temperature [3]. Therefore it has been anticipated that  $\Phi_{TS}$  for anthracenes depends on temperature as long as  $T_2$  lies below  $S_1$ .

In this article, we study the temperature effect on the inverse intersystem crossing of some halogenated anthracenes to confirm the above anticipation and to establish the mechanism of inverse intersystem crossing.

<sup>†</sup>Present address: Government Industrial Research Institute Osaka, Midorigaoka 1, Ikeda, Osaka 563, Japan.

<sup>‡</sup>Author to whom correspondence should be addressed.



## 2. Experimental details

The stepwise two-photon excitation technique has been described elsewhere [1]. A microsecond flash lamp is first fired to populate  $T_1$  uniformly in a sample cell and a  $Q$ -switched ruby laser is repeatedly fired to excite  $T_1$  into  $T_n$ . Fluorescence was observed with an RCA 1P28 photomultiplier and a Tektronix 7844-7A92, 7B92 oscilloscope through an aqueous copper(II) sulphate solution filter and a Narumi RM-23 monochromator. The energy of the laser pulse was measured with a GenTec ED-100 joulemeter.

Anthracene, 9-methylanthracene (9-MA), 9,10-dichloroanthracene (9,10-DCA) and 9,10-dibromoanthracene (9,10-DBA) are the same materials as studied in previous work [1 - 3]. 1,5-Dichloroanthracene (1,5-DCA) was synthesized from 1,5-dichloroanthraquinone according to Brienne and Jacques [4], and purified by repeated recrystallization from toluene and by vacuum sublimation. Ethanol (99.5%; G.R. grade, Wako Junyaku) was used as received. All sample solutions were degassed by repeated bulb-to-trap distillation. The temperature was controlled by circulating cold dry nitrogen gas or water around the sample cell.

## 3. Results and discussion

Figure 1 shows the energy diagrams for the anthracenes studied. The  $T_1$  levels have already been determined [5, 6]. The  $T_2$ - $T_1$  energy gaps were determined from the 0-0 bands of the  $T_2 \leftarrow T_1$  absorption spectra shown in Fig. 2. The  $T_2 \leftarrow T_1$  absorption of 9-MA has been reported to be structureless in the near-IR region [7]. However, it has a very weak band at  $12\,100\text{ cm}^{-1}$  as shown in Fig. 2(b), which is attributed to the 0-0 band of  $T_2 \leftarrow T_1$  absorption. The energy diagrams are consistent with the  $T_2 \rightarrow T_1$  fluorescence spectra [8] and with either the temperature dependence of fluorescence [7, 9, 10] or the triplet yield [7, 11].

The excitation of  $T_1$  state molecules by a laser pulse gives rise to fluorescence from the  $S_1$  state. Its time-integrated total fluorescence intensity  $F$  is given by

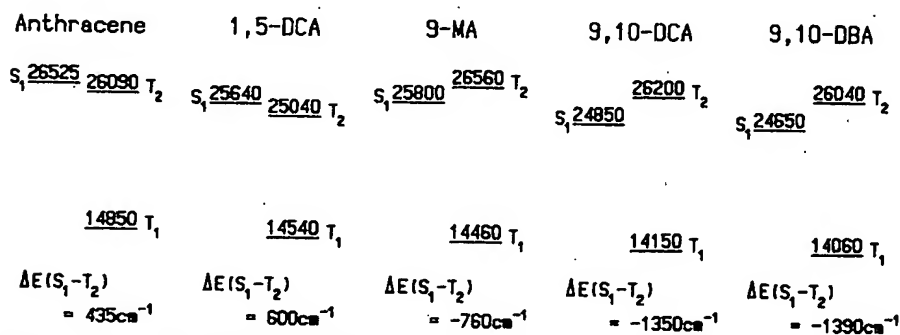


Fig. 1. Energy level diagrams of anthracenes in ethanol (energies in inverse centimetres).

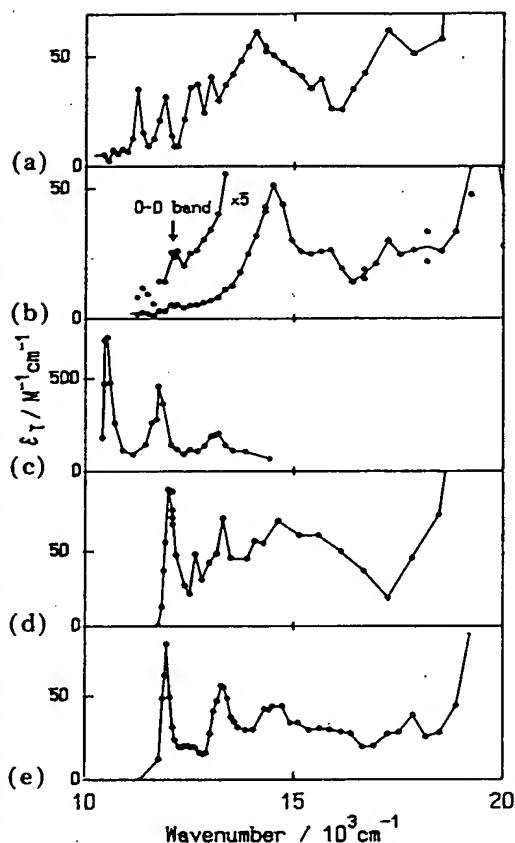


Fig. 2. T-T absorption spectra of anthracenes in ethanol: (a) anthracene; (b) 9-MA; (c) 1,5-DCA; (d) 9,10-DCA; (e) 9,10-DBA.

$$F = \alpha \Phi_F \sigma N_T \int I(t) dt \quad (1)$$

where  $\alpha$  is a constant depending on the experimental conditions,  $\Phi_F$  is the normal fluorescence yield,  $\sigma$  is the apparent absorption cross-section of a  $T_1$  molecule in units of square centimetre per molecule,  $N_T$  is the number of  $T_1$  molecules in inverse cubic centimetres, and  $\int I(t) dt$  is the laser intensity in photons per square centimetre. The  $\sigma$  values at 298 K have already been reported [2] except that for 1,5-DCA. The  $\sigma$  value for 1,5-DCA was determined to be  $6.4 \times 10^{-23} \text{ cm}^2 \text{ molecule}^{-1}$  by comparing  $F$  with the time-integrated fluorescence intensity due to simultaneous two-photon absorption [1]. Then we used the two-photon absorption cross-section of  $\delta = 4.8 \times 10^{-51} \text{ cm}^4 \text{ s photon}^{-1} \text{ molecule}^{-1}$  for 1,5-DCA.

Under the condition  $\int I(t) dt = \text{constant}$ ,  $F$  is almost proportional to the absorbance  $D_T$  of the  $T_n \leftarrow T_1$  absorption at  $22\,730 \text{ cm}^{-1}$  as shown in Fig. 3, because the extinction coefficients of  $T_n \leftarrow T_1$  absorption are small at  $14\,400 \text{ cm}^{-1}$ , the wavenumber of ruby laser light.

Figure 3 also shows the temperature effect on  $F$  for 1,5-DCA.  $\alpha$  is regarded as a constant, because the spectral change in fluorescence and the change in refractive index of the solvent are negligible in the temperature

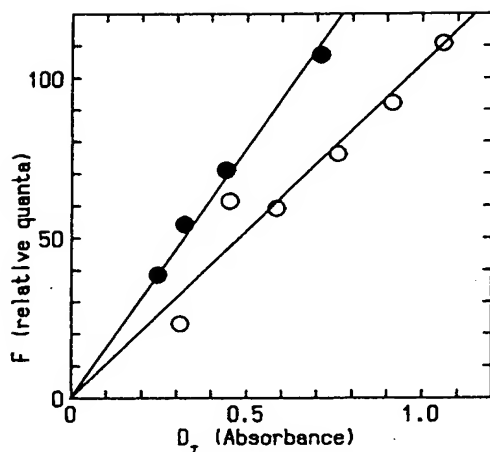


Fig. 3. Plots of  $F$  vs. the absorbance  $D_T$  at  $22\,730\text{ cm}^{-1}$  for T-T absorption of 1,5-DCA: ○, 200 K; ●, 296 K.

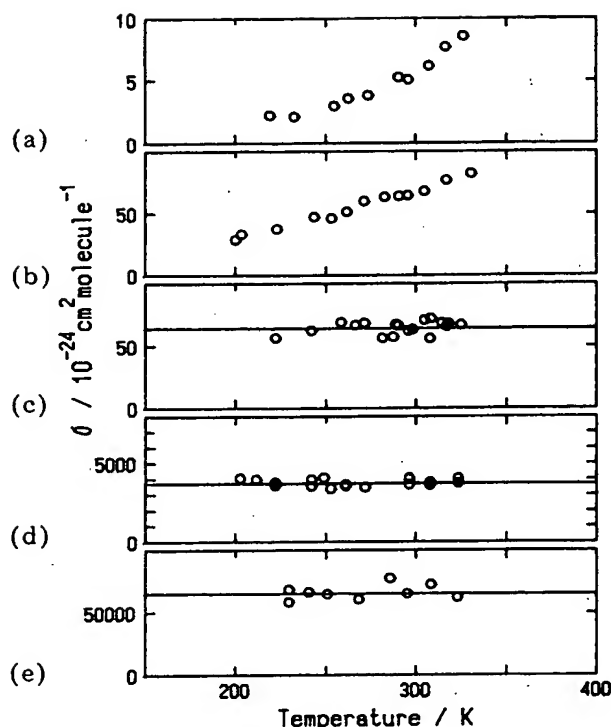


Fig. 4. Temperature dependence of  $\sigma$ : (a) anthracene; (b) 1,5-DCA; (c) 9-MA; (d) 9,10-DCA; (e) 9,10-DBA.

range studied. Thus the temperature dependence of the slope may be attributed to the temperature dependence of  $\sigma$  and  $\Phi_F$ . Kearvell and Wilkinson [9] and Bowen and Sahu [10] found that the temperature dependence of  $\Phi_F$  for anthracenes was approximately described by

$$\Phi_F = \frac{k_F}{k_F + k_1 + k_2 \exp(-E_{ST}/k_B T)} \quad (2)$$

The values for  $k_F$ ,  $k_1$ ,  $k_2$  and  $E_{ST}$  are calculated from their results. Using eqn. (2) we can distinguish the temperature dependence of  $\sigma$  from that of  $\Phi_F \sigma$ .

Figure 4 shows the temperature dependence of  $\sigma$ . For anthracene and 1,5-DCA  $\sigma$  depends on temperature but for the others it does not. These facts are indicative of the importance of the location of  $T_2$ , because the energy level of  $T_2$  is lower than that of  $S_1$  for anthracene and 1,5-DCA and vice versa for the *meso* derivatives.

$\sigma$  may be described in the general form [1, 2]

$$\sigma = \Phi_{SS}\sigma_{ST} + \Phi_{TS}\sigma_{TT} \quad (3)$$

where  $\Phi_{SS}$  and  $\Phi_{TS}$  are the quantum yields for the  $S_m \rightarrow S_1$  internal conversion and the  $T_n \rightarrow S_m$  inverse intersystem crossing, and  $\sigma_{ST}$  and  $\sigma_{TT}$  are the absorption cross-sections in units of square centimetres per molecule for the

$S_m \leftarrow T_1$  and  $T_n \leftarrow T_1$  absorptions. As the  $S_m \rightarrow S_1$  internal conversion is much faster than the other transitions,  $\Phi_{SS}$  is usually assumed to be unity. However,  $\Phi_{SS}\sigma_{ST}$  is considered to be too small to participate in  $\sigma$  except for the case of 9,10-DBA [12], because the  $S_m \leftarrow T_1$  absorption is a spin-forbidden transition. Since the value of  $\sigma_{TT}$  for 1,5-DCA is  $2.5 \times 10^{-19} \text{ cm}^2 \text{ molecule}^{-1}$  at  $14\,400 \text{ cm}^{-1}$  in ethanol, the  $\Phi_{TS}$  value for 1,5-DCA is determined to be  $2.6 \times 10^{-4}$  at 298 K. The  $\Phi_{TS}$  values at 298 K are summarized in Table 1.

Both  $\sigma_{ST}$  and  $\sigma_{TT}$  change only slightly with temperature so that the temperature dependence of  $\sigma$  may be attributed to the temperature dependence of  $\Phi_{TS}$  alone. When  $T_n$  is populated by the excitation of  $T_1$  with  $14\,400 \text{ cm}^{-1}$  laser light, the energy gap between  $T_n$  and  $T_2$  is much smaller than that between  $T_2$  and  $T_1$ . Then the  $T_n \rightarrow T_2$  internal conversion will be much faster than the  $T_2 \rightarrow T_1$  internal conversion. Therefore it is most probable that the  $T_n \rightarrow S_1$  intersystem crossing occurs through  $T_2$ , and  $\Phi_{TS}$  is described as follows:

$$\Phi_{TS} = \frac{k_{TS}}{k_{TT} + k_{TS}} \quad (4)$$

where  $k_{TS}$  and  $k_{TT}$  are the rate constants for the  $T_2 \rightarrow S_1$  intersystem crossing and the  $T_2 \rightarrow T_1$  internal conversion respectively. In the case of the *meso* derivatives the  $T_2$  level is higher than the  $S_1$  level so that  $k_{TS}$  will not depend on temperature. In fact,  $\Phi_{TS}$  for the *meso* derivatives does not depend on temperature as shown in Figs. 4(c) - 4(e). In contrast, in the cases of anthracene and 1,5-DCA the  $T_2$  level is lower than the  $S_1$  level so that  $k_{TS}$  may depend on temperature if the vibrational thermalization in  $T_2$  is instantly achieved. As the condition  $\Phi_{TS} \ll 1$  holds for the cases of anthracene and 1,5-DCA, eqn. (4) is reduced to

$$\Phi_{TS} = k_{TS}/k_{TT} \quad (5)$$

The average rate of inverse intersystem crossing from  $T_2$  to  $S_1$  may be given by

$$k_{TS} = \sum_v A(T_{2,v} - S_1) \exp\left(-\frac{E_v}{k_B T}\right) / \sum_v \exp\left(-\frac{E_v}{k_B T}\right) \quad (6)$$

where  $E_v$  is the vibrational energy of  $T_2$  and  $A(T_{2,v} - S_1)$  is the frequency factor for the inverse intersystem crossing from a vibrationally excited state of  $T_2$  to the  $S_1$  state. If it is assumed that (i)  $A(T_{2,v} - S_1)$  is a constant  $A_{TS}$  for  $E_v > \Delta E (> 0)$  and zero for  $E_v < \Delta E$  and that (ii) the energy difference between  $E_n$  and  $E_{n-1}$  is much less than  $k_B T$ , eqn. (6) becomes the Arrhenius equation

$$k_{TS} = A_{TS} \exp\left(-\frac{\Delta E}{k_B T}\right) \quad (7)$$

Since  $\Phi_{SS}\sigma_{ST}$  can be neglected for the cases of anthracene and 1,5-DCA, we finally obtain from eqns. (3), (5) and (7)

TABLE 1  
Numerical parameters for inverse intersystem crossing of anthracenes

	$\Phi_{TS}$ at 298 K	$A_{TS}/k_{TT}$ or $k_{TS}/k_{TT}$	$\Delta E$ ( $\text{cm}^{-1}$ )	$\Delta E(S_1-T_2)$ ( $\text{cm}^{-1}$ )	$A_{ST}^a$ ( $\text{s}^{-1}$ )	$k_{TT}^b$ ( $\text{s}^{-1}$ )	$k_{TT}^c$ ( $\text{s}^{-1}$ )
Anthracene	$2.6 \times 10^{-5}^d$	$7.2 \times 10^{-4}$	690	435	$3.4 \times 10^9$	$4.7 \times 10^{12}$	$3.7 \times 10^{12}$
1,5-DCA	$2.6 \times 10^{-4}$	$1.5 \times 10^{-3}$	360	600	$1.5 \times 10^9$	$1.0 \times 10^{11}$	$4 \times 10^{12}^e$ $6.5 \times 10^{11}$
9-MA	$3.6 \times 10^{-4}^d$	$3.6 \times 10^{-4}$	0	-760	$4.9 \times 10^9$	$1.4 \times 10^{13}$	$8 \times 10^{11}^e$
9,10-DCA	$1.5 \times 10^{-2}^d$	$1.5 \times 10^{-2}$	0	-1350	$7.2 \times 10^{10}$	$4.8 \times 10^{12}$	$> 4.9 \times 10^{12}$
9,10-DBA	$1.9 \times 10^{-1}^f$	$2.3 \times 10^{-1}$	0	-1390	$9.1 \times 10^{11}$	$4.0 \times 10^{12}$	— $1.4 \times 10^{11}$

<sup>a</sup> From refs. 9 and 10.

<sup>b</sup> Calculated on the assumption  $A_{TS} = A_{ST}$  or  $k_{TS} = A_{ST}$ .

<sup>c</sup> Calculated according to the procedure described in ref. 8.

<sup>d</sup> From ref. 2.

<sup>e</sup> From ref. 8.

<sup>f</sup> From ref. 12.

$$\ln \Phi_{TS} = \ln\left(\frac{\sigma}{\sigma_{TT}}\right) = \ln\left(\frac{A_{TS}}{k_{TT}}\right) - \frac{\Delta E}{k_B T} \quad (8)$$

The results shown in Figs. 4(a) and 4(b) are satisfactorily analysed by eqn. (8) as shown in Fig. 5. From the slopes and intercepts we obtain the values for  $\Delta E$  and  $A_{TS}/k_{TT}$ . They are listed in Table 1. The  $\Delta E$  value agrees reasonably with the energy gap  $\Delta E(S_1-T_2)$  between  $S_1$  and  $T_2$  in the cases of anthracene and 1,5-DCA.

It was confirmed that (i)  $\Phi_{TS}$  depends on temperature when  $S_1$  is located above  $T_2$  and does not when  $T_2$  is located above  $S_1$  and that (ii) in the former case the activation energy of inverse intersystem crossing is close to the energy gap between  $S_1$  and  $T_2$ . Therefore it is concluded that the inverse intersystem crossing of anthracenes occurs predominantly from the thermalized  $T_2$  state to the  $S_1$  state.

In the cases of 9-MA and 9,10-DCA, the condition  $\Phi_{TS} \ll 1$  is also valid so that the following equation holds to a good approximation:

$$\sigma = \sigma_{TT} k_{TS}/k_{TT} \quad (9)$$

Using the values for  $\sigma$  and  $\sigma_{TT}$  listed in Table 1 we obtain the values for  $k_{TS}/k_{TT}$ , which are also listed in Table 1.

In the case of 9,10-DBA the value for  $\Phi_{SS}\sigma_{ST}$  is 0.83 times the value for  $\Phi_{TS}\sigma_{TT}$  at  $14\,400\text{ cm}^{-1}$  [12] so that  $\Phi_{TS}\sigma_{TT}$  is evaluated to be  $3.6 \times 10^{-20}\text{ cm}^2\text{ molecule}^{-1}$ . Using  $\sigma_{TT} = 1.6 \times 10^{-19}\text{ cm}^2\text{ molecule}^{-1}$  at  $14\,400\text{ cm}^{-1}$  and eqn. (4) we obtain  $k_{TS}/k_{TT} = 0.23$ .

Figure 6 shows plots of  $\log(A_{TS}/k_{TT})$  and  $\log(k_{TS}/k_{TT})$  vs.  $\log(\Sigma\zeta^2)$ , where  $\Sigma\zeta^2$  is the sum of the squares of the atomic spin-orbit coupling factors [13-15]. A linear relationship between  $A_{TS}/k_{TT}$  or  $k_{TS}/k_{TT}$  and  $\Sigma\zeta^2$  indicates the presence of a heavy-atom effect on the inverse ( $T_2 \rightarrow S_1$ ) intersystem crossing. A slight deviation for anthracene from this relation is within

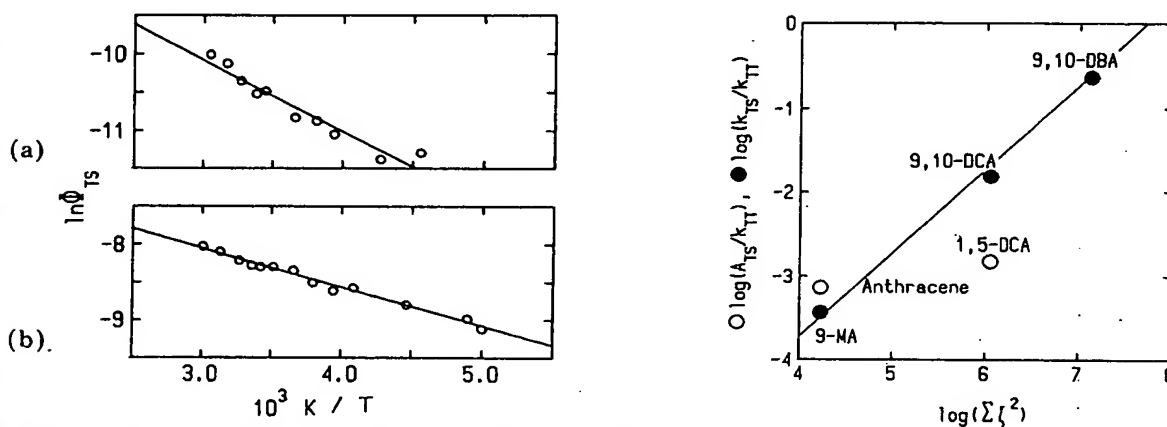


Fig. 5. Plots of  $\ln \Phi_{TS}$  vs.  $1/T$ : (a) anthracene; (b) 1,5-DCA.

Fig. 6. Plots of  $\log(A_{TS}/k_{TT})$  and  $\log(k_{TS}/k_{TT})$  vs.  $\log(\Sigma\zeta^2)$ . (The slope of the full line is unity.)

the experimental error limit. The  $A_{TS}/k_{TT}$  value for 1,5-DCA is only 0.1 times the  $k_{TS}/k_{TT}$  value for 9,10-DCA. This may be due to the difference in the atomic orbital coefficients of molecular orbitals responsible for the spin-orbit coupling between  $S_1$  and  $T_2$ . The non-radiative decay rate of  $T_1$  is 4 times larger for 9,10-DCA than for 1,5-DCA [15]. The pre-exponential factor of temperature-dependent intersystem crossing is 30 times larger for 9,10-DCA than for 1,5-DCA [10]. These results support the above concept. If the heavy-atom effect influences  $k_{TS}$  and  $A_{TS}$  alone, the good linearity observed for the *meso* derivatives may suggest only a slight difference in the lifetime of  $T_2$  among them. The pre-exponential factors  $A_{ST}$  for the temperature-dependent  $S_1 \rightarrow T_1$  intersystem crossing have been determined by Kearvel and Wilkinson [9]. In order to estimate the values for  $k_{TT}$  we assume  $A_{TS} = A_{ST}$  or  $k_{TS} = A_{ST}$ . The  $k_{TT}$  values are listed in Table 1. Certainly all the  $k_{TT}$  values thus obtained are in the range of  $10^{12} - 10^{13} \text{ s}^{-1}$ .

Gillispie and Lim [8] measured the quantum yields of  $T_2 \rightarrow T_1$  fluorescence for many anthracenes and further evaluated the decay rates of  $T_2$  for anthracene and 1,5-DCA, which are listed in Table 1. They then used the radiative decay rates from  $T_2$  to  $T_1$  which were evaluated from the integrated  $T_2 \leftarrow T_1$  absorption spectra. Since the  $T_2 \leftarrow T_1$  absorption spectra of 9-MA and 9,10-DBA in addition to those of anthracene and 1,5-DCA have now been measured, the  $k_{TT}$  values can be evaluated for these *meso* derivatives and are listed in Table 1. The agreement between the  $k_{TT}$  values obtained according to the two different methods is very good except for 9,10-DBA. It is noted, however, that the  $k_{TT}$  values are two or three orders of magnitude larger than the decay rates of  $T_2$  which have been determined by Liu and coworkers [16, 17] from a study of the photosensitized reaction of olefins in solvents such as benzene and hexane. As revealed by Pineault *et al.* [18] the decay rates reported by Liu and coworkers are too small to explain the decay rate of greater than about  $10^{11} \text{ s}^{-1}$  for the  $T_2$  state of 9-iodoanthracene, because the decay rate is not considered to vary markedly among the *meso* derivatives, judging from the energy gap between  $T_2$  and  $T_1$ . In order to determine the decay rates of  $T_2$  Liu and coworkers assumed a diffusion-controlled energy transfer from the second excited triplet state of the anthracenes to the ground state of the olefin even for olefin concentrations above 0.1 M. However, their assumption is not necessarily valid, because non-stationary quenching may not be negligible in solvents such as benzene and hexane at quencher concentrations above 0.1 M. Therefore, it is assumed that the lifetime determined by them is an overestimation. In order to determine whether or not the non-stationary quenching is operative at olefin concentrations above 0.1 M and to measure the real lifetime of  $T_2$ , further experiments are required.

### Acknowledgment

We thank Miss Chieko Iwanaga for the purification of anthracenes.

## References

- 1 S. Kobayashi, K. Kikuchi and H. Kokubun, *Chem. Phys. Lett.*, **42** (1976) 494.
- 2 S. Kobayashi, K. Kikuchi and H. Kokubun, *Chem. Phys.*, **27** (1978) 399.
- 3 H. Fukumura, K. Kikuchi and H. Kokubun, *Chem. Phys. Lett.*, **92** (1982) 29.
- 4 M. J. Brienne and J. Jacques, *Bull. Soc. Chim. Fr.*, **1** (1973) 190.
- 5 M. R. Padhye, S. P. McGlynn and M. Kasha, *J. Chem. Phys.*, **24** (1956) 588.
- 6 D. F. Evans, *J. Chem. Soc.*, (1957) 1351.
- 7 R. G. Bennett and P. J. McCartin, *J. Chem. Phys.*, **44** (1966) 1969.
- 8 G. D. Gillispie and E. C. Lim, *Chem. Phys. Lett.*, **63** (1979) 355.
- 9 A. Kearvell and F. Wilkinson, *J. Chim. Phys. (Paris) Special Edition, Transitions Non-radiatives dans les Molecules*, 1970, p. 125.
- 10 E. J. Bowen and J. Sahu, *J. Phys. Chem.*, **63** (1959) 4.
- 11 E. C. Lim, J. D. Laposa and J. M. H. Yu, *J. Mol. Spectrosc.*, **19** (1966) 412.
- 12 K. Kikuchi, H. Fukumura and H. Kokubun, *Chem. Phys. Lett.*, **123** (1986) 226.
- 13 D. S. McClure, *J. Chem. Phys.*, **17** (1949) 905.
- 14 D. S. McClure, *J. Chem. Phys.*, **20** (1952) 682.
- 15 S. P. McGlynn, T. Azumi and M. Kinoshita, *Molecular Spectroscopy of the Triplet State*, Prentice-Hall, Englewood Cliffs, NJ, 1969, p. 261.
- 16 R. S. H. Liu and J. R. Edman, *J. Am. Chem. Soc.*, **91** (1969) 1492.
- 17 R. O. Campbell and R. S. H. Liu, *J. Am. Chem. Soc.*, **95** (1973) 6560.
- 18 R. L. Pineault, C. G. Morgante and W. S. Struve, *J. Photochem.*, **17** (1981) 435.



## Reverse intersystem crossing from a triplet state of rose bengal populated by sequential 532- + 1064-nm laser excitation

J.M. Larkin <sup>a,b</sup>, W.R. Donaldson <sup>a</sup>, T.H. Foster <sup>b,c,\*</sup>, R.S. Knox <sup>a,b</sup>

<sup>a</sup> Laboratory for Laser Energetics, University of Rochester, 250 East River Road, Rochester, NY 14623, USA

<sup>b</sup> Department of Physics and Astronomy, University of Rochester, Rochester, NY 14627, USA

<sup>c</sup> Department of Radiology, University of Rochester School of Medicine and Dentistry, Rochester, NY 14642, USA

Received 4 December 1998

### Abstract

A previously unstudied triplet state of rose bengal has been identified by near-infrared laser flash photolysis measurements. Its absorption peaks between 1050 and 1075 nm with a cross-section of  $(1.1 \pm 0.1) \times 10^{-16} \text{ cm}^2$  in phosphate-buffered saline. This state, denoted as  $T_2$ , was further characterized through two-step laser-induced fluorescence measurements. The photophysical parameters describing the higher-lying triplet populated by the two-step, two-color excitation were determined from fits of a model of the kinetics to the experimental data. This model allows reverse intersystem crossing from  $T_2$  to  $S_1$  followed by  $S_1 \rightarrow S_0$  fluorescence. On the basis of this analysis  $T_2$  has a quantum yield of reverse intersystem crossing of  $0.0142 \pm 0.0003$ , a lifetime of  $5.8 \pm 1.6 \text{ ps}$ , and a thermalization rate constant of  $1.30 \pm 0.18 \text{ ps}^{-1}$ . © 1999 Elsevier Science B.V. All rights reserved.

**Keywords:** Triplet state; Rose bengal; Laser excitation

### 1. Introduction

Although intersystem crossing has been identified primarily with transitions from the lowest excited singlet state of a molecule to an even lower-lying triplet state, triplet to singlet intersystem crossing also may occur. Well-known examples of reverse (triplet to singlet) intersystem crossing include E- and P-type delayed fluorescence [1]. E-type delayed

fluorescence, also known as delayed thermal fluorescence, is observed when thermal activation causes population transfer from  $T_1$  back to the more energetic  $S_1$  state. The strength of E-type delayed fluorescence is temperature dependent, and its lifetime reflects that of  $T_1$ . P-type delayed fluorescence results when the activation energy is provided by triplet–triplet annihilation ( $T_1 + T_1 \rightarrow S_1 + S_0$ ). The strength of the P-type delayed fluorescence increases quadratically with the triplet concentration.

Reverse intersystem crossing may also occur from higher-lying triplet states where intersystem crossing to the singlet manifold competes with direct internal conversion to the lowest triplet state. This process of

\* Corresponding author. University of Rochester, School of Medicine and Dentistry, Department of Radiology, 601 Elmwood Avenue, Box 648, Rochester, NY 14642, USA. Fax: +1-716-273-1033; E-mail: thfoster@optics.rochester.edu

reverse intersystem crossing from higher-lying triplets is responsible for two-step laser-induced fluorescence (TSLIF) observed in several dyes [2–6]. The quantum yield of reverse intersystem crossing,  $\Phi_{\text{isc}}$ , can be quite small ( $< 10^{-5}$ ) [2,3], but there are reports of exceptionally high yields ( $\Phi_{\text{isc}} > 0.1$ ) in 9,10-dibromoanthracene [4], several merocyanine derivatives [5], tetraphenylporphyrin [6], erythrosin B [6], and rose bengal [6].

Several reports of reverse intersystem crossing in rose bengal (RB) have been published [6–8]. Durán and Cilento [7] describe observations of fluorescence following generation of RB triplets by energy transfer from excited triplet acetone. It was believed that higher-lying triplets were populated through triplet-triplet excitation transfer and subsequently relaxed to  $S_1$  through reverse intersystem crossing. The magnitude of the emission was compared for a series of xanthene dyes (fluorescein, eosin, and rose bengal), which revealed that heavy-atom substitution enhanced the effect. This process was not associated with a particular triplet state, and no attempt was made to quantify its yield. Ketsle et al. [8] investigated transient absorption changes following two-pulse excitation (532 nm + 694 nm) of various fluorescein derivatives, including rose bengal, incorporated in polymer hosts. Photobleaching of the  $T_1$  absorption due to the second pulse was observed to have a component that was irreversible on the microsecond time scale. It was observed that the decrease in concentration of  $T_1$  equaled the increase in concentration of  $S_0$ , providing evidence for a photo-physical rather than photochemical process. Fluorescence emission was also observed coincident with the second pulse. A reverse intersystem crossing quantum yield of 0.72 was reported for  $T_3$ , the triplet state excited by red light. Most recently, the work of Reindl and Penzkofer [6] reported an 80% quantum yield of reverse intersystem crossing for  $T_4$ , the state excited through absorption of green light by  $T_1$ . Using a model of the population dynamics, the yield was extracted from measurements of the pulse-to-pulse variation in fluorescence for a train of picosecond pulses.

The present work is the first study to identify and investigate the properties of  $T_2$ , a triplet state in rose bengal populated by near-infrared light ( $\lambda = 1064$  nm). We have used laser flash photolysis and two-

step laser-induced fluorescence measurements to determine the triplet-triplet absorption cross-section spectrum in the near infrared and the quantum yield of reverse intersystem crossing and lifetime of  $T_2$ . In addition, upper limits on the reverse intersystem crossing yield for  $T_3$  are established.

## 2. Experimental

The foundation of the laser system is a mode-locked Nd:YAG laser that generates a train of pulses at 76 MHz. Every 400 ms a single pulse is selected using an electro-optic switch and amplified using a regenerative amplifier followed by a flashlamp-pumped two-pass amplifier (both Nd:YAG). The amplified pulses have a wavelength of 1064 nm, a pulse length of  $\sim 190$  ps, and energies exceeding 2 mJ. The second harmonic is generated from this pulse using a KDP crystal, resulting in a pulse with a wavelength of 532 nm, a pulse length of  $\sim 134$  ps, and an energy greater than 250  $\mu$ J.

The experimental setup for the laser flash photolysis measurements is shown in Fig. 1 using the symbols defined in Table 1. In this configuration the second-harmonic pulse ( $\lambda = 532$  nm) is separated from the fundamental by dichroic mirror DM with any residual light at the fundamental wavelength ( $\lambda = 1064$  nm) further attenuated by filter F. The majority of this frequency-doubled pump pulse is focused by cylindrical lens CL onto the masked sample cuvette, exciting a 2-mm by 1-cm cross-sectional area. A small fraction of the pump pulse is reflected by glass plate BS prior to the cylindrical lens, attenuated by neutral density filters, and then

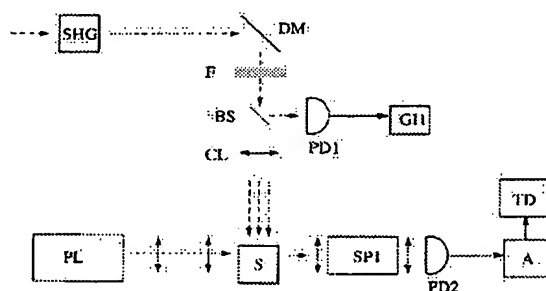


Fig. 1. Experimental setup for laser flash photolysis measurements. See Table 1 for symbol definitions.

Table 1  
Equipment used in the laser flash photolysis and two-step laser-induced fluorescence experiments

	Description	Manufacturer, model
A	fast amplifier	EG & G, 574
BS	glass plate (microscope slide)	
CL	cylindrical lens	
DM	dichroic mirror, R@532 nm, T@1064 nm	
F	short-pass filter	Schott, KG3
GI1-4	gated integrator	Stanford Research Systems, 250
L1-3	lenses	
P	prism	
PD1-2	silicon photodiodes	EG & G, FND-100
PL	mercury lamp; fast shutter; long-pass filter	Vincent Associates, Uniblitz VS25; Schott, RG695
PMT	photomultiplier tube	Burle, 6199
PS	polarizing beam splitter	
S	sample cuvette and beam mask	
SHG	second harmonic generator (KDP crystal)	
SP1	monochromator, bandwidth ~ 13 nm	Instruments SA, H20
SP2	monochromator, bandwidth ~ 4 nm	Photon Technology, 102
TD	digitizing oscilloscope	Hewlett-Packard, HP54201A
WP	half-wave plate ( $\lambda = 1064$ nm)	

detected by silicon photodiode PD1. This signal is captured by gated integrator GI1 and transferred to a computer. By removing the sample cuvette and placing an energy meter behind the beam mask, the pump pulse monitor signal measured by PD1 can be calibrated with respect to the energy reaching the sample. Transient absorption changes are probed by a broadband light beam traveling along the length of the irradiated zone (perpendicular to the pump pulse). The probe pulse has a 20-ms duration and is produced by a mercury lamp followed by a long-pass filter and fast mechanical shutter. This collection of elements is represented by PL in Fig. 1. The probe pulse passes through monochromator SP1 before being detected by silicon photodiode PD2. The photodiode signal is increased by multistage amplifier A and then recorded by digital oscilloscope TD. The average signal from 64 shots at 9-bit resolution is then transferred to a computer for analysis.

The two-step laser-induced fluorescence measurements probing  $T_2$  are made with the optical layout shown in Fig. 2. To achieve a high degree of spectral separation between the fundamental and second-harmonic pulses, prism P is used to spatially disperse the two beams. The first pump pulse (P1) has a wavelength of 532 nm and the second pump pulse (P2) has a wavelength of 1064 nm. P2 is delayed by

34 ns relative to P1 by traversal of a greater optical path length. The delay path includes a half-wave

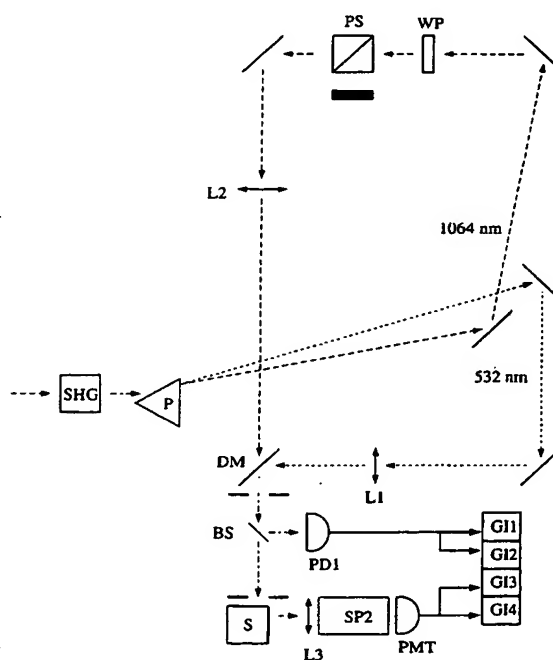


Fig. 2. Experimental setup for two-step laser-induced fluorescence measurements. See Table 1 for symbol definitions.

plate followed by a polarizing beam splitter, allowing for continuous variation of the second pump pulse energy. The pump pulses, P1 and P2, are recombined spatially at dichroic mirror DM. The pulses pass through two pin holes, ensuring collimation, before irradiating a 2-mm diameter spot at the sample cuvette. As in the laser flash photolysis layout, a small fraction of the excitation light is reflected by a glass plate to a silicon photodiode. This signal is split before sampling by two gated integrators, GI1 and GI2, which distinguish between the P1 and P2 signals. The pump-pulse signals are calibrated individually using an energy meter. Emission from the excited sample is collected, spectrally resolved using monochromator SP2, and detected by a photomultiplier tube. The signal from the PMT is split and sampled by the gated integrators GI3 and GI4. The temporal gate of GI3 is centered on the fluorescence excited by P1. The center of the GI4 temporal gate is set to be 34 ns later than the center of the GI3 gate, corresponding to the time delay between the pump pulses. Both gates are 20 ns wide. The values of all four gated integrators are recorded by a computer for each shot.

Two-step laser-induced fluorescence measurements probing  $T_3$  are made using a similar setup. In this case P2, the 1064-nm pump pulse, is replaced by a 632-nm-wavelength pump pulse, while the first pump pulse remains at 532 nm. The 632-nm pulse is generated by stimulated Raman scattering of the Nd:YAG second harmonic in an 18-cm ethanol cell, resulting in 60  $\mu\text{J}/\text{pulse}$  with a pulse length of approximately 80 ps. The 632-nm light is separated from the 532-nm light by a pair of prisms before P2 enters the delay line. The pulses are spatially recombined at the dichroic mirror DM, and from this point the system is identical to the previously described two-step, laser-induced fluorescence apparatus.

Rose bengal was purchased from Sigma (St. Louis, MO) and used without further purification. All experiments were carried out in phosphate-buffered saline with a pH of 7. Effects of photobleaching were minimized by continuously stirring all samples with a micro-stirbar during irradiation. Photobleaching was monitored by measuring the decrease in fluorescence as a function of the number of excitation pulses. There was less than a 5% decrease in fluorescence after more than 3700 two-step excita-

tions. Samples had a concentration of approximately 20  $\mu\text{M}$  and were stored in the dark prior to use.

### 3. Analysis

Several photophysical parameters associated with an upper triplet state can be determined from two-step laser-induced fluorescence (TSLIF) measurements collected over a range of second pump pulse (P2) fluences. These measurements are sensitive to the lifetime of the upper triplet state excited by P2, the quantum yield of intersystem crossing from this state back to the singlet manifold, and its thermalization rate. The upper triplet photophysical parameters are determined by fitting a model of the two-step laser-induced fluorescence process to the fluence-dependent TSLIF data.

The kinetic model used to analyze the TSLIF experiments is shown in Fig. 3. The rate equations describing this model are

$$\begin{aligned}
 \frac{dp_{S_0}}{dt} &= -\sigma_{S_0S_1}(p_{S_0} - p_{S'_1})I_1(t) \\
 &\quad + (1 - \Phi_{isc})\tau_{S'_1}^{-1}p_{S_1} + \tau_{T_1}^{-1}p_{T_1} \\
 \frac{dp_{T_1}}{dt} &= \Phi_{isc}\tau_{S'_1}^{-1}p_{S_1} - \tau_{T_1}^{-1}p_{T_1} \\
 &\quad - \sigma_{T_1T_4}(p_{T_1} - p_{T_4})I_1(t) \\
 &\quad - \sigma_{T_1T_n}(p_{T_1} - p_{T'_n})I_2(t) \\
 &\quad + (1 - \Phi_{isc,T_4})\tau_{T_4}^{-1}p_{T_4} \\
 &\quad + (1 - \Phi_{isc,T_n})\tau_{T_n}^{-1}p_{T_n} \\
 \frac{dp_{S_1}}{dt} &= k_r p_{S'_1} - \tau_{S_1}^{-1}p_{S_1} \\
 \frac{dp_{S'_1}}{dt} &= \sigma_{S_0S_1}(p_{S_0} - p_{S'_1})I_1(t) - k_r p_{S'_1} \\
 &\quad + \Phi_{isc,T_4}\tau_{T_4}^{-1}p_{T_4} + \Phi_{isc,T_n}\tau_{T_n}^{-1}p_{T_n} \quad (1) \\
 \frac{dp_{T_n}}{dt} &= k_{r,T_n} p_{T'_n} - \tau_{T_n}^{-1}p_{T_n} \\
 \frac{dp_{T'_n}}{dt} &= \sigma_{T_1T_n}(p_{T_1} - p_{T'_n})I_2(t) - k_{r,T_n} p_{T'_n} \\
 \frac{dp_{T_4}}{dt} &= \sigma_{T_1T_4}(p_{T_1} - p_{T_4})I_1(t) - \tau_{T_4}^{-1}p_{T_4}
 \end{aligned}$$

where the  $p_i$  are the populations of  $S_0$ ,  $T_1$ ,  $S_1$ ,  $S'_1$ ,  $T_n$ ,  $T'_n$ , and  $T_4$  (arranged in order of increasing

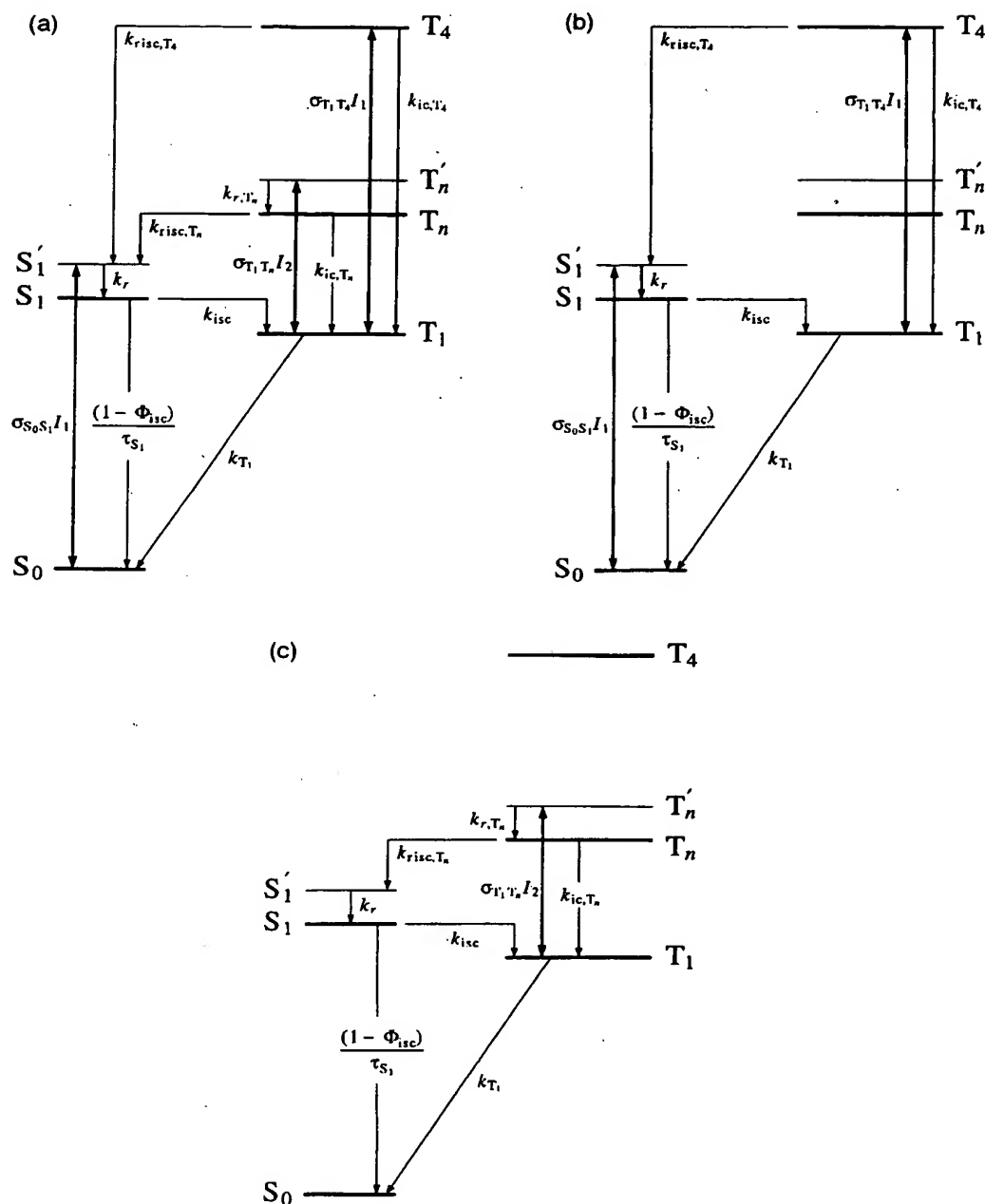


Fig. 3. Energy-level scheme for description of two-color excitation dynamics. (a) Complete two-step model, (b) P1 subset of model, (c) P2 subset of model. See Table 2 for parameter descriptions and values.

energy), where  $n = 2$  or  $3$ . Table 2 lists the definitions and values of the photophysical parameters.

The effects of oxygen quenching have been included in  $\tau_{T_1}$ . The unknown parameters are  $\Phi_{risc, T_n}$ ,  $\tau_{T_n}$ , and

Table 2  
Parameters used in the two-step laser-induced fluorescence model for rose bengal

Parameter	Description	Value	Ref.
$\sigma_{S_0S_1}$	ground state absorption cross-section at 532 nm ( $S_0 + \hbar\omega \rightarrow S'_1$ )	$1.8 \times 10^{-16} \text{ cm}^2$	[9]
$\sigma_{T_1T_2}$	triplet absorption cross-section ( $T_1 + \hbar\omega \rightarrow T'_2$ )	$(1.1 \pm 0.1) \times 10^{-16} \text{ cm}^2$	This work
$\sigma_{T_1T_4}$	triplet absorption cross-section at 532 nm ( $T_1 + \hbar\omega \rightarrow T_4$ )	$7.4 \times 10^{-17} \text{ cm}^2$	[9]
$\tau_{S_1}$	$S_1$ lifetime	89 ps	[9–11]
$\tau_{T_1}$	lifetime of $T_1$ (includes both phosphorescence and oxygen-quenching)	3 $\mu\text{s}$	[12]
$\tau_{T_4}$	lifetime of $T_4$	50 fs	[9]
$\tau_{T_n}$	lifetime of $T_n$	fitting parameter	
$\Phi_{isc}$	intersystem crossing yield ( $S_1 \rightarrow T_1$ )	0.98	[11,12]
$\Phi_{isc,T_4}$	reverse intersystem crossing yield ( $T_4 \rightarrow S'_1$ )	0.8	[6]
$\Phi_{isc,T_n}$	reverse intersystem crossing yield ( $T_n \rightarrow S'_1$ )	fitting parameter	
$F_1$	first pump pulse fluence ( $\lambda = 532 \text{ nm}$ )	$(8.8 \pm 0.5) \times 10^{15} \text{ photons/cm}^2$	
$F_2$	second pump pulse fluence ( $\lambda = 1064 \text{ nm}$ )	varied	
$k_{ic,T_4}$	internal conversion rate constant ( $T_4 \rightarrow T_1$ )	$(1 - \Phi_{isc,T_4})/\tau_{T_4}$	
$k_{ic,T_n}$	internal conversion rate constant ( $T_n \rightarrow T_1$ )	$(1 - \Phi_{isc,T_n})/\tau_{T_n}$	
$k_{isc}$	intersystem crossing rate constant	$\Phi_{isc}/\tau_{S_1}$	
$k_{r,T_n}$	thermalization rate constant ( $T'_n \rightarrow T_n$ )	fitting parameter	
$k_r$	thermalization rate constant ( $S'_1 \rightarrow S_1$ )	$10^{12} \text{ s}^{-1}$	[9]
$k_{isc,T_4}$	reverse intersystem crossing rate constant ( $T_4 \rightarrow S'_1$ )	$\Phi_{isc,T_4}/\tau_{T_4}$	
$k_{isc,T_n}$	reverse intersystem crossing rate constant ( $T_n \rightarrow S'_1$ )	$\Phi_{isc,T_n}/\tau_{T_n}$	
$k_{T_1}$	$T_1$ relaxation rate constant	$1/\tau_{T_1}$	

$k_{r,T_n}$ . The pump pulses P1 and P2 have a gaussian temporal profile such that

$$I_1(t) = \frac{F_1}{\sqrt{2\pi\delta_1^2}} \exp\left(-\frac{(t + \Delta/2)^2}{2\delta_1^2}\right) \quad (2)$$

and

$$I_2(t) = \frac{F_2}{\sqrt{2\pi\delta_2^2}} \exp\left(-\frac{(t - \Delta/2)^2}{2\delta_2^2}\right), \quad (3)$$

where  $F_1$  and  $F_2$  are the fluences,  $\delta_1$  and  $\delta_2$  are related to the full width at half-maximum pulse lengths by  $\text{FWHM} = \sqrt{8 \ln 2} \delta$ , and  $\Delta$  is the time delay between the peaks of P1 and P2.

Excited-state absorption from states other than  $T_1$  has been neglected. Previous experiments have found no evidence for absorption of 532-nm light by  $S_1$  [9]. The state  $T_4$  may absorb 532-nm light and thus populate an even higher-lying state, but we assume with Reindl and Penzkofer [6] that any such extremely high-lying state will relax back to  $T_4$  immediately. This process would affect transmission measurements, but since the present studies are concerned only with emission, it appears reasonable to omit it in this case. Finally, absorption by  $T_n$  is also not included in this model. The validity of this assumption will be discussed in Section 4.

As a result of the large time delay between the pump pulses ( $\Delta = 34 \text{ ns}$ ), it is possible to separate the system of rate equations (Eq. (1)) into two subsets. The set of equations describing the effects of the first pump pulse is

$$\begin{aligned}
 \frac{dp_{S_0}}{dt} &= -\sigma_{S_0S_1}(p_{S_0} - p_{S'_1})I_1(t) \\
 &\quad + (1 - \Phi_{isc})\tau_{S_1}^{-1}p_{S_1} + \tau_{T_1}^{-1}p_{T_1} \\
 \frac{dp_{T_1}}{dt} &= \Phi_{isc}\tau_{S_1}^{-1}p_{S_1} - \tau_{T_1}^{-1}p_{T_1} \\
 &\quad - \sigma_{T_1T_4}(p_{T_1} - p_{T_4})I_1(t) \\
 &\quad + (1 - \Phi_{isc,T_4})\tau_{T_4}^{-1}p_{T_4} \\
 \frac{dp_{S_1}}{dt} &= k_r p_{S'_1} - \tau_{S_1}^{-1}p_{S_1} \\
 \frac{dp_{S'_1}}{dt} &= \sigma_{S_0S_1}(p_{S_0} - p_{S'_1})I_1(t) - k_r p_{S'_1} \\
 &\quad + \Phi_{isc,T_4}\tau_{T_4}^{-1}p_{T_4} \\
 \frac{dp_{T_4}}{dt} &= \sigma_{T_1T_4}(p_{T_1} - p_{T_4})I_1(t) - \tau_{T_4}^{-1}p_{T_4},
 \end{aligned} \quad (4)$$

which are used for  $t = -\infty$  to  $t = 0$ . The time  $t = 0$  is midway between the peaks of P1 and P2, which

are separated by a delay much greater than their pulse lengths and the lifetimes of all excited states except  $T_1$ . The processes included in this first segment, where only the effects of P1 are relevant, are shown in Fig. 3b. This set of equations describing the effects of P1 neglects all terms containing  $I_2$ . Since  $T_n$  and  $T'_n$  are only populated by P2, corresponding terms can be eliminated from Eq. (1) since  $p_{T_n} = p_{T'_n} = 0$ . The process of reverse intersystem crossing is included in this model of the interaction of P1 with the sample. The first pump pulse may be absorbed by both  $S_0$  and by any  $T_1$  population created by preceding parts of the same pulse. Absorption of P1 light by the  $T_1$  state populates the  $T_4$  state, which has been shown to have a high yield of reverse intersystem crossing [6]. It is necessary to include this process for pulses longer than the  $S_1 \rightarrow T_1$  intersystem crossing time since it can lead to an apparent enhancement of the fluorescence yield, particularly at fluences resulting in depletion of the ground state. At the P1 fluence used experimentally, the solution of Eq. (4) that includes the reverse intersystem crossing process led to a 29%-greater integrated fluorescence compared to an otherwise identical set of equations that neglected this process. It is important to emphasize that the reverse intersystem crossing described above occurs from the triplet state populated by secondary absorption of the first pump pulse and is easily distinguished temporally from the process this experiment is designed to measure: reverse intersystem crossing from the triplet state populated by the second pump pulse.

The effects of P1 and P2 can be separated cleanly since the system has relaxed such that only  $S_0$  and  $T_1$  are populated at  $t = 0$ . The effects of only the second pump pulse are considered from this time to  $t = +\infty$ . The model of this second excitation step is shown in Fig. 3c. The equations describing this segment are

$$\frac{dp_{S_0}}{dt} = (1 - \Phi_{isc})\tau_{S_1}^{-1}p_{S_1} + \tau_{T_1}^{-1}p_{T_1}$$

$$\begin{aligned} \frac{dp_{T_1}}{dt} = & \Phi_{isc}\tau_{S_1}^{-1}p_{S_1} - \tau_{T_1}^{-1}p_{T_1} \\ & - \sigma_{T_1T_n}(p_{T_1} - p_{T'_n})I_2(t) \\ & + (1 - \Phi_{isc,T_n})\tau_{T_n}^{-1}p_{T_n} \end{aligned}$$

$$\frac{dp_{S_1}}{dt} = k_r p_{S_1} - \tau_{S_1}^{-1}p_{S_1} \quad (5)$$

$$\frac{dp_{S'_1}}{dt} = -k_r p_{S'_1} + \Phi_{isc,T_n}\tau_{T_n}^{-1}p_{T_n}$$

$$\frac{dp_{T_n}}{dt} = k_{r,T_n}p_{T'_n} - \tau_{T_n}^{-1}p_{T_n}$$

$$\frac{dp_{T'_n}}{dt} = \sigma_{T_1T_n}(p_{T_1} - p_{T'_n})I_2(t) - k_{r,T_n}p_{T'_n}$$

In this segment all terms containing  $I_1$  and  $p_{T_4}$ , the population of  $T_4$ , are dropped from Eq. (1).

The fluorescence  $f$  due to the two pulses is proportional to the population of  $S_1$  such that

$$f_1 = \frac{\Phi_f}{\tau_{S_1}} \int_{-\infty}^0 p_{S_1}(t) dt \quad (6)$$

and

$$f_2 = \frac{\Phi_f}{\tau_{S_1}} \int_0^{+\infty} p_{S_1}(t) dt \quad (7)$$

where  $\Phi_f$  is the fluorescence yield. The two-step laser-induced fluorescence ratio  $f_R$  is defined by

$$f_R \equiv \frac{f_2}{f_1} \quad (8)$$

This is a convenient quantity to compare with experimental results since fluorescence yield, collection, and detection efficiency factors are eliminated.

The  $T_n$  photophysical parameters are determined by fitting this model of the two-step laser-induced fluorescence process to the fluence-dependent  $f_R$  obtained experimentally. As will be discussed later, extraction of the parameters requires  $f_R$  measurements over a range of P2 fluences, which, at the upper limit, are sufficient to partially deplete the lowest triplet state. In addition, the length of the second pump pulse must exceed the lifetime of  $T_n$ . A numerical approach is required since under these conditions analytical solutions cannot be obtained easily. The numerical analysis consists of three major components: (a) a calculation of the fluence-dependent  $f_R$  for a given set of  $T_n$  photophysical parameters, (b) an algorithm that optimizes these parameters to provide the best fit to the experimental data, and (c) an estimate of the precision to which

the extracted parameters are known based on a randomization and re-optimization technique.

Calculation of the fluence-dependent, two-step laser-induced fluorescence ratio was based on the sequential solution of the rate equations given in Eqs. (4) and (5). These rate equations were solved using Runge–Kutta numerical integration. The agreement between the  $f_R$  obtained from this model and the experimental data can be quantified by the  $\chi^2$  statistic:

$$\chi^2 = \frac{1}{N} \sum_{(F_1, F_2)} \left( \frac{f_{R, \text{expt}}(F_1, F_2) - f_{R, \text{model}}(F_1, F_2; k_{r, T_n}, \tau_{T_n}, \Phi_{\text{risc}, T_n})}{\sigma_{R, \text{expt}}(F_1, F_2)} \right)^2, \quad (9)$$

which is summed over the set  $(F_1, F_2)$  for which experimental measurements of the TSLIF ratio,  $f_{R, \text{expt}}$ , were made. The standard deviations of those measurements are given by  $\sigma_{R, \text{expt}}$ . The next step is to search parameter space in order to find the values of  $k_{r, T_n}$ ,  $\tau_{T_n}$ , and  $\Phi_{\text{risc}, T_n}$  that minimize  $\chi^2$ . The optimization algorithm used is the downhill simplex method [13].

The downhill simplex method will find the set of parameters that minimizes  $\chi^2$ , but it does not report the precision with which these parameters are known given the uncertainties in the experimental measurements. This precision was estimated by running the optimization routine on sets of TSLIF ratio measurements,  $f_{R, \text{mix}}$ , calculated from

$$f_{R, \text{mix}}(F_1, F_2) = f_{R, \text{expt}}(F_1, F_2) + r \sigma_{R, \text{expt}}(F_1, F_2), \quad (10)$$

where  $r$  is a uniformly distributed random number between  $-1$  and  $1$ . The standard deviations of the parameters found in minimizing ten such data sets provide the estimated precision to which the parameters are known.

An analytical model of two-step laser-induced fluorescence that is limited to low-intensity and low-fluence conditions can be developed. In this regime the fluorescence signals are given by

$$f_1 = a \sigma_{S_0 S_1} F_1 \quad (11)$$

and

$$f_2 = a \Phi_{\text{isc}} \Phi_{\text{risc}, T_n} \sigma_{S_0 S_1} F_1 \sigma_{T_1 T_n} F_2, \quad (12)$$

where  $a$  includes fluorescence yield, collection, and detection factors. Calculating the two-step laser-induced fluorescence ratio from Eqs. (11) and (12) gives

$$f_R = \Phi_{\text{isc}} \Phi_{\text{risc}, T_n} \sigma_{T_1 T_n} F_2. \quad (13)$$

Although this expression cannot be used to determine  $\tau_{T_n}$  and  $k_{r, T_n}$ , it is useful for estimating upper limits on  $\Phi_{\text{risc}, T_n}$  when there is an undetectable two-step laser-induced fluorescence signal.

## 4. Results

The triplet–triplet absorption spectrum of rose bengal in the near infrared (Fig. 4) is derived from a series of transient absorption measurements acquired by laser flash photolysis. There is no measurable ground state absorption in this region. Detector insensitivity prevented the extension of this spectrum beyond 1100 nm. Using the intensity variation method [14] it was found that the absorption has a peak between 1050 and 1075 nm with a cross-section  $\sigma_{T_1 T_2} = (1.1 \pm 0.1) \times 10^{-16} \text{ cm}^2$ .

Fig. 5 shows two-step laser-induced fluorescence results for  $T_2$ . The ratio of two-step to one-step

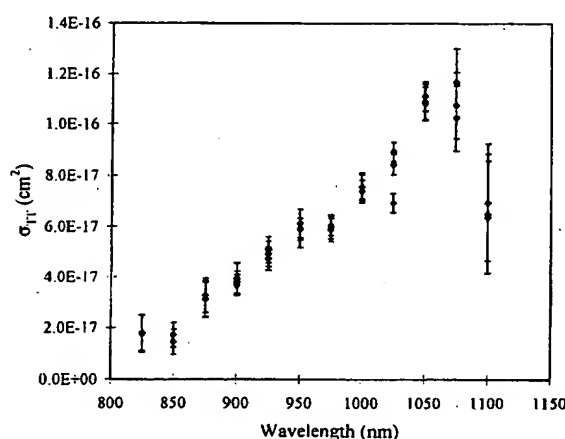


Fig. 4. Triplet–triplet absorption spectrum of rose bengal in the near infrared.



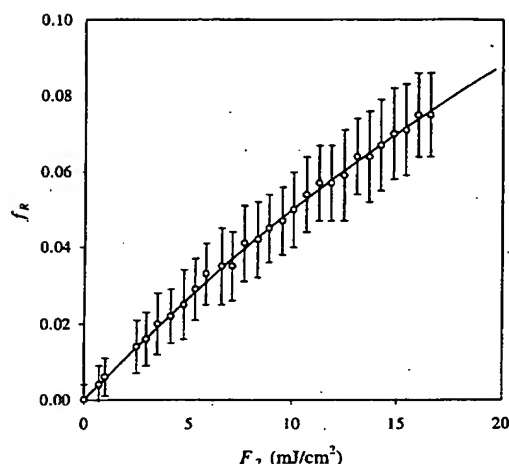


Fig. 5. Fluence dependence of two-step laser-induced fluorescence ratio  $f_R$ . Delay between excitation pulses: 34 ns. Circles are averages of from 26 to 370 double-pulse excitations with error bars indicating the standard deviations. The curve represents the best fit ( $\chi^2 = 0.011$ ) calculated from solutions of Eqs. (4) and (5) using the parameter values given in Table 2. The photophysical parameters determined from the fitting procedure are  $\Phi_{\text{risc},T_2} = 0.0142 \pm 0.0003$ ,  $\tau_{T_2} = 5.8 \pm 1.6$  ps, and  $k_{r,T_2} = 1.30 \pm 0.18$  ps $^{-1}$ .

fluorescence  $f_{R,\text{expt}}$  versus the fluence of the second pump pulse ( $\lambda_2 = 1064$  nm) is plotted. The first pump-pulse fluence ( $\lambda_1 = 532$  nm) was held approximately constant at  $3.3 \pm 0.2$  mJ/cm $^2$ , and the resulting one-step fluorescence varied by less than 2%. No emission following P2 was detected when P1 was blocked. Each point in this plot represents the average of from 26 to 370 double-pulse excitations. The error bars indicate the corresponding standard deviations. In addition, the spectrum of the 532-nm + 1064-nm excited emission was measured and found to be the same as the  $S_1 \rightarrow S_0$  fluorescence spectrum, confirming that the TSLIF results from repopulation of  $S_1$ . The parameters  $\Phi_{\text{risc},T_2}$ ,  $\tau_{T_2}$ , and  $k_{r,T_2}$  can be determined by analyzing the nonlinear dependence of  $f_R$  on  $F_2$  using the multistate kinetic model described in Section 3. This analysis of the data shown in Fig. 5 gives,  $\Phi_{\text{risc},T_2} = 0.0142 \pm 0.0003$ ,  $\tau_{T_2} = 5.8 \pm 1.6$  ps, and  $k_{r,T_2} = 1.30 \pm 0.18$  ps $^{-1}$  with  $\chi^2 = 0.011$ .

Similar measurements probing  $T_3$  ( $\lambda_1 = 532$  nm,  $\lambda_2 = 632$  nm) failed to detect any two-step laser-induced fluorescence. Based on the fluorescence detec-

tion limits, the quantum yield of reverse intersystem crossing from  $T_3$  can be constrained to  $\Phi_{\text{risc},T_3} < 0.06$  using Eq. (13) with  $\sigma_{T_1,T_3}$  determined from Ref. [15] and  $f_R$  set equal to the uncertainty in the TSLIF measurement.

## 5. Discussion

Although no analytical expression can be given for  $f_R(F_1, F_2)$  that is applicable for the high fluences used in these experiments, it is possible to explain qualitatively the shape of the  $f_R$  versus  $F_2$  curve shown in Fig. 5. This explanation also provides some justification for why the kinetic model analysis is sensitive to the lifetime and thermalization rate of the upper triplet state. Under low-fluence and low-intensity conditions, Eq. (13) predicts that  $f_R$  will increase linearly with  $F_2$ . Deviations from the predicted linear response are expected to occur for P2 with sufficiently high intensity or fluence. When the pulse length is shorter than the lifetime of  $T_2$ , the saturation fluence  $F_{\text{sat}} = (\sigma_{T_1,T_2})^{-1}$  for  $T_1 \rightarrow T_2$  excitation is  $9 \times 10^{15}$  photons/cm $^2$  (1.7 mJ/cm $^2$ ). Multiple excitations are possible, however, for pulses that are longer than the lifetime of  $T_2$ . This allows the two-step laser-induced fluorescence ratio to continue to grow beyond the short-pulse saturation fluence limit. Limits on the growth of the two-step laser-induced fluorescence are not solely fluence dependent. The maximum rate at which population can be excited to the upper-triplet state is limited by the thermalization rate constant  $k_{r,T_2}$ . In addition, the maximum number of excitation cycles that can be achieved during a pulse is limited by the upper-triplet lifetime  $\tau_{T_2}$  and the length of the second pump pulse  $\delta_2$ . Since the nonlinear portion of the  $f_R$  curve is dependent on the upper-triplet lifetime and its thermalization rate, it is possible to extract these parameters from a fit of the kinetic model to data obtained under high-intensity and high-fluence conditions where the deviation from linearity becomes significant.

The multistate kinetic model described in Eq. (1) and Fig. 3 is not the only possible explanation for fluorescence following 532-nm + 1064-nm excitation. An alternative model that deserves consideration includes absorption of 1064-nm light by  $T_2$  to

populate  $T_4$ , a state already known to have a high reverse intersystem crossing yield [6]. On the basis of energetic considerations, the  $T_2 \rightarrow T_4$  absorption process appears to be plausible, although restrictions such as those based on parity may disallow this transition. If reverse intersystem crossing were to occur predominantly from  $T_4$ , then the expression for  $f_R$  given in Eq. (13) should be modified to give

$$f_R = \Phi_{isc} \Phi_{isc,T_4} \sigma_{T_1,T_2} \sigma_{T_2,T_4} F_2^2. \quad (14)$$

According to this model,  $f_R$  increases quadratically rather than linearly in  $F_2$  since population of  $T_4$  from  $T_1$  requires the sequential absorption of two 1064-nm photons. In addition,  $f_R$  is expected to saturate at a value greater than  $\Phi_{isc} \Phi_{isc,T_4} = 0.78$ . The experimental data shown in Fig. 5 do not exhibit this behavior, which justifies our elimination of this alternative model.

Although it has been observed previously by Ketsle et al. [8], no two-step laser-induced fluorescence was detected in our 532-nm + 632-nm experiment. We believe our non-detection is due to the fact that this experiment was performed under conditions much less favorable than for the 532-nm + 1064-nm experiment. Both the maximum P2 fluence and the triplet–triplet absorption cross-section were significantly less at 632 nm compared to 1064 nm. Even with these limitations, however, the value of can be determined to be less than 0.06. This result disagrees with a yield of 0.72 for this state reported previously [8].

Ketsle et al. attempted to measure the yield of reverse intersystem crossing through measurements of the change in  $T_1$  absorption (and therefore, concentration) in a two-step excitation experiment [8]. Immediately following P2, a decrease in the concentration  $\Delta C_{ab}$  of  $T_1$  was observed, which was followed by a partial recovery  $\Delta C_{ac}$ , as shown in Fig. 6. Fig. 6 is a sketch showing the key features in the transient signal plotted in Fig. I of Ref. [8]. The lack of complete recovery is due to reverse intersystem crossing from the higher-lying triplet populated by P2. From these concentration changes Ketsle et al. calculated the reverse intersystem crossing yield using the formula

$$\frac{\Delta C_{ac}}{\Delta C_{ab}} = \Phi_{isc,T_3}. \quad (15)$$

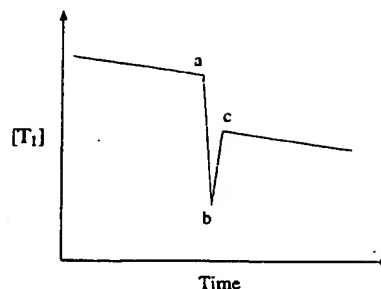


Fig. 6. Schematic of transient changes in  $T_1$  concentration (based on Fig. I in Ref. [8]).

Eq. (15) attributes the bleaching to the entire fraction undergoing reverse intersystem crossing. It is more appropriate, however, to interpret bleaching as due to the fraction that undergoes reverse intersystem crossing and in addition does not repopulate the triplet manifold through  $S_1 \rightarrow T_1$  transfer, implying

$$\frac{\Delta C_{ac}}{\Delta C_{ab}} = \Phi_{isc,T_3}(1 - \Phi_{isc}). \quad (16)$$

Indeed, this latter interpretation of the bleaching fraction agrees with that used by Redmond et al. [5]. Recalculating a yield based on Eq. (16) using the Ketsle et al. bleaching fraction data found in Table I of Ref. [8] gives  $\Phi_{isc,T_3} \gg 1$ . Since this quantum yield cannot exceed unity, it appears that their experimental data was obtained under conditions in which the assumptions used to derive these equations do not apply. In particular, these equations are valid only under conditions in which  $\Delta C_{ab}$  is proportional to the number of photons absorbed by  $T_1$ . This can only occur when the length of the exciting pulse is shorter than the lifetime of the upper-triplet state ( $\delta_2 \ll \tau_{T_3}$ ) and when the transient absorption detection system is capable of responding on this same time scale. Ketsle et al. do not report the length of their second pump pulse, but state only that it is from a ruby laser. It appears likely that their excitation pulse is longer than several nanoseconds, which is much greater than the expected upper-triplet lifetime of picoseconds or less. In addition, the time response of their transient absorption detection system is not reported. The use of long pulses or slow detection systems with this transient absorption technique will

lead to an underestimate of the number of absorbed photons, thus leading to values of  $\Phi_{\text{nisc},T_3}$  that exceed unity. The equipment requirements are not as demanding for fluorescence methods of measuring reverse intersystem crossing.

Reverse intersystem crossing yields have been calculated for a growing number of molecules. An aspect of this study that makes it of particular interest is that these yields have now been measured for several triplet states of rose bengal. Previous workers in this field have suggested that population excited to  $T_n$  relaxes rapidly to the next-lowest triplet state and that the triplet-singlet transfer is predominantly due to reverse intersystem crossing from this less-energetic state [6,16]. According to this model, the reverse intersystem crossing yield should be independent of the high-lying triplet state initially excited; experimental measurements clearly contradict this prediction with high yields of  $\Phi_{\text{nisc},T_4} = 0.80$  if  $T_4$  is initially excited [6], to much lower yields of  $\Phi_{\text{nisc},T_2} = 0.0142$  for the case of direct population of  $T_2$  (measured in this work).

To understand these results it is instructive to consider the energies of the relevant triplet and singlet states. The energies of the singlet states can be estimated from the peaks of the ground-state absorption spectrum. Similarly, the energies of the triplet states relative to  $T_1$  can be estimated from triplet-triplet absorption spectra (the present work and Refs. [17,18]). The energy of  $T_1$  in methanol is 1.75 eV [19]. These results have been compiled in Table 3. The energy gaps between the excited triplet states and the nearest less energetic singlet state are  $\Delta E(T_2S_2) = 0.51$  eV,  $\Delta E(T_3S_3) = 0.35$  eV, and  $\Delta E(T_4S_4) = 0.08$  eV. Thus we find that the transition with the smallest energy gap exhibits the greatest reverse intersystem crossing yield ( $\Phi_{\text{nisc},T_2} = 0.0142$ ,  $\Phi_{\text{nisc},T_3} < 0.06$ ,  $\Phi_{\text{nisc},T_4} = 0.80$ ). Although this ordering is consistent with a simple interpretation of the energy gap law for nonradiative transitions, which states that reverse intersystem crossing is likely to be most favorable when there is a small energy gap between the triplet state and a nearby singlet, such an interpretation must be considered critically. As developed by Englman and Jortner [20], the energy gap law applies to a particular triplet-singlet pair, whereas here we are considering three such pairs. The strength of the spin-orbit coupling between dif-

Table 3  
Energies of rose bengal excited states

State	Energy (eV)	Ref.
$S_1$	2.10	This work
$S_2$	2.41	This work
$S_3$	3.51	This work
$S_4$	3.95	This work
$T_1$	1.75	[19]
$T_2$	2.92	This work
$T_3$	3.86	[17]
$T_4$	4.03	[18]

Singlet-state energies are estimated from the ground state absorption spectrum.

Triplet-state energies are estimated from the  $T_1$  absorption spectrum.

ferent states may vary by several orders of magnitude. Since we do not know the values of the coupling parameters for the three transitions under consideration, it is impossible to definitively attribute the entire variation in reverse intersystem crossing yield to differences in the energy gap.

## 6. Conclusion

We have presented what we believe to be the first study of a triplet state of rose bengal that is produced by 1064-nm excitation of  $T_1$ . The triplet-triplet absorption cross-section was measured between 825 nm and 1100 nm. This state was further characterized using two-step laser-induced fluorescence to determine its thermalization rate constant, lifetime, and quantum yield of reverse intersystem crossing. Similar two-step laser-induced fluorescence measurements were made of the triplet excited by 632-nm light.

In earlier work, the reverse intersystem crossing yield was predicted to be independent of which higher-lying triplet state was initially excited. The present work finds that the yields for triplets excited by red and near-infrared light,  $T_3$  and  $T_2$ , are much less than those reported earlier for the more-energetic state  $T_4$ , which is populated by green light [6]. An analysis of the triplet-triplet absorption spectrum and the ground-state absorption spectrum shows that  $T_4$  is energetically close to a state in the singlet

manifold, whereas the corresponding gaps are significantly greater for  $T_2$  and  $T_3$ .

### Acknowledgements

This work has been supported by the US Department of Energy Office of Inertial Confinement Fusion under Cooperative Agreement Number DE-FC03-92SF19460, the University of Rochester, the New York State Energy Research and Development Authority, and by US Public Health Service grant CA68409. The support of DOE does not constitute an endorsement by DOE of the views expressed in this article.

### References

- [1] S.P. McGlynn, T. Azumi, M. Kinoshita, *Molecular spectroscopy of the triplet state*, Prentice-Hall, Englewood Cliffs, NJ, 1969.
- [2] S. Kobayashi, K. Kikuchi, H. Kokubun, *Chem. Phys. Lett.* 42 (1976) 494.
- [3] S. Kobayashi, K. Kikuchi, H. Kokubun, *Chem. Phys.* 27 (1978) 399.
- [4] W.G. McGimpsey, J.C. Scaiano, *J. Am. Chem. Soc.* 111 (1989) 335.
- [5] R.W. Redmond, I.E. Kochevar, M. Krieg, G. Smith, W.G. McGimpsey, *J. Phys. Chem. A* 101 (1997) 2773.
- [6] S. Reindl, A. Penzkofer, *Chem. Phys.* 211 (1996) 431.
- [7] N. Durán, G. Cilento, *Photochem. Photobiol.* 32 (1980) 113.
- [8] G.A. Ketsle, L.V. Levshin, S.N. Letuta, *Opt. Spectrosc. (USSR)* 68 (1990) 202.
- [9] H. Stiel, K. Teuchner, A. Paul, D. Leupold, I.E. Kochevar, *J. Photochem. Photobiol. B: Biol.* 33 (1996) 245.
- [10] G.R. Fleming, A.W.E. Knight, J.M. Morris, R.J.S. Morrison, G.W. Robinson, *J. Am. Chem. Soc.* 99 (1977) 4306.
- [11] M.A.J. Rodgers, *Chem. Phys. Lett.* 78 (1981) 509.
- [12] P.C.C. Lee, M.A.J. Rodgers, *Photochem. Photobiol.* 45 (1987) 79.
- [13] W.H. Press, S.A. Teukolsky, W.T. Vetterling, B.P. Flannery, *Numerical Recipes in FORTRAN: The Art of Scientific Computing*, Cambridge Univ. Press, Cambridge, 1992.
- [14] I. Carmichael, G.L. Hug, *J. Phys. Chem. Ref. Data* 15 (1986) 1.
- [15] P. Murasecco-Suardi, E. Gassmann, A.M. Braun, E. Oliveros, *Helv. Chim. Acta* 70 (1987) 1760.
- [16] H. Fukumura, K. Kikuchi, K. Koike, H. Kokubun, *J. Photochem. Photobiol. A: Chem.* 42 (1988) 283.
- [17] G. Smith, W.G. McGimpsey, M.C. Lynch, I.E. Kochevar, R.W. Redmond, *Photochem. Photobiol.* 59 (1994) 135.
- [18] C.R. Lambert, H. Stiel, D. Leupold, M.C. Lynch, I.E. Kochevar, *Photochem. Photobiol.* 63 (1996) 154.
- [19] T. Shen, Z.-G. Zhao, Q. Yu, H.-J. Xu, *J. Photochem. Photobiol. A: Chem.* 47 (1989) 203.
- [20] R. Englman, J. Jortner, *Mol. Phys.* 18 (1970) 145.

# Structure of the triplet excited state of bromanil from time-resolved resonance Raman spectra and simulation

Mrinalini Puranik<sup>a)</sup> and Siva Umapathy<sup>b)</sup>

*Department of Inorganic and Physical Chemistry, Indian Institute of Science, Bangalore-560012, India*

Jaap G. Snijders

*Theoretical Chemistry, Materials Science Centre, Rijksuniversiteit Groningen, Nijenborgh 4, 9747 AG Groningen, The Netherlands*

Jayaraman Chandrasekhar

*Department of Organic Chemistry, Indian Institute of Science, Bangalore-560012, India*

(Received 29 May 2001; accepted 9 July 2001)

Time-resolved resonance Raman (TR3) spectroscopy has been used to study the structure of the triplet excited state of bromanil. These experimental results were then simulated using parameters from density functional theoretical (DFT) calculations and wave packet dynamics, in order to understand the structure and mode-specific displacements of the resonant excited state. The transition dipole moments and the energy separation of the  $T_1$  and  $T_n$  states were obtained from time-dependent DFT calculations. We have demonstrated application of the technique to tetrabromo-*p*-benzoquinone. From our calculations, the observed  $T_1 \rightarrow T_n$  absorption spectrum has been assigned to the  ${}^3B_g \rightarrow {}^3B_u$  transition. The geometry has been optimized for the resonant higher triplet state,  $T_n$ , and is found to be in good agreement with the predictions of the wave packet dynamical simulations. Mode-specific displacements of the triplet state geometry have been obtained from simulations and these have been rationalized with respect to the molecular orbital involved. Thus, we have demonstrated that from the simulations of the experimental TR3 spectral data, valuable additional information can be derived on the structure of the transient states that may then be used for elucidation of structure-reactivity correlation in the future. © 2001 American Institute of Physics. [DOI: 10.1063/1.1398304]

## I. INTRODUCTION

Time-resolved resonance Raman spectroscopy is a sensitive technique that has been demonstrated to be useful in addressing a wide range of chemical problems due to its electronic state and chromophoric selectivity.<sup>1-4</sup> It has been used to study electron transfer, transient intermediate kinetics and structure-reactivity relationships to name a few. While the experimental methodologies have progressed considerably in terms of both the varying time scales and the types of phenomenon addressed, the theoretical support has been generally directed towards the calculation of vibrational frequencies using quantum chemical methods. These are then used to obtain a better understanding of the structure and to support assignments of observed bands. However, little interpretation of the observed intensities in the excited state is made. This paper attempts to address the lacuna in utilizing the information contained in the intensities. In the ground state resonance Raman (RR) studies, the frequencies of the observed bands have been used to derive information on the structure, whereas the intensities have been utilized to under-

stand the mode specific dynamics on the resonant excited state potential energy surface (PES), particularly near the Franck-Condon region.<sup>5-13</sup>

Generally, the time-dependent theory of resonance Raman intensities, originally put forth by Lee and Heller<sup>5</sup> has been applied with much success. The dynamics of a wide range of fast chemical processes involving, e.g., bacteriorhodopsin,<sup>6</sup> stilbene,<sup>7,8</sup> azodyes,<sup>9-11</sup> chlorine dioxide,<sup>12</sup> *N*-methylacetamide,<sup>13</sup> etc., has been probed. Application of the time-dependent theory of resonance Raman intensities to molecules in their ground state has been reviewed extensively.<sup>6,14-18</sup> Two approaches are generally used: (i) The molecular parameters may come from a purely empirical model, and these are then optimized iteratively to obtain the best fit to the observed spectra,<sup>6-12,14-18</sup> or (ii) molecular parameters are obtained from *ab initio* calculations and the Raman intensities are predicted and compared with experiment.<sup>13,19-21</sup> The former method allows a direct interpretation of the observed intensities and the latter is more likely to be used to judge the reliability of various computational methods. Our group has applied the former method to trans-azobenzene<sup>9,10</sup> in order to understand the dynamics of isomerization. The technique was also developed further to obtain the vibrational and solvent reorganization energies from the total reorganization energy.<sup>11</sup> The success of these wave packet dynamical methods in the ground state molecules spurred attempts to apply the theory for

<sup>a)</sup>Also at: Department of Organic Chemistry, Indian Institute of Science, Bangalore-560012, India.

<sup>b)</sup>Author to whom correspondence should be addressed.  
Phone: +91-(0)80-3601234, Fax: +91-(0)80-3601552.  
Electronic mail:umapathy@ipc.iisc.ernet.in

short-lived transient intermediates like radical cations<sup>19,20</sup> and triplet excited states<sup>21</sup> that are experimentally observed using time-resolved resonance Raman spectroscopy. These developments are important for most organic photochemical processes, including in quinones, in which the photoreactive state is the lowest triplet state. Thus the knowledge of the mode-specific dynamics of the triplet excited state is essential to understand the reactivity. It is also important to know the nature of the potential energy surface of the higher triplet state in the Franck-Condon region. While some information on the structure of the lowest triplet state ( $T_1$ ) is obtained from the time-resolved resonance Raman spectra as well as *ab initio* and DFT calculations, it is more difficult to determine properties of the potential energy surfaces of higher triplet states.

Previous attempts by Wilbrandt and co-workers<sup>21</sup> to predict triplet excited-state Raman spectra involved an *ab initio* calculation of the optimized geometry of the transient state (e.g.,  $T_1$ ). This was followed by a CI calculation to obtain the transition dipole moment of the  $T_1 \rightarrow T_n$  transition, where  $T_n$  denotes the resonant triplet state. Displacements in equilibrium geometries between the  $T_1$  and  $T_n$  states were computed. These were used to predict Raman spectra, which were compared with the experimentally observed spectra. Similar procedures were followed for radical cations as well.<sup>19,21</sup> This approach gave a satisfactory agreement between the calculated and experimentally determined resonance Raman spectra. However, for larger polyatomics, CI calculations rapidly become computationally intractable. It is also desirable that the experimentally measured intensities should be used to extract information on the PES in a more direct way rather than by comparison of predicted and observed spectra alone.

Recently, several studies have demonstrated the success of density functional theoretical techniques in the prediction of vibrational frequencies.<sup>22–28</sup> Accurate normal mode descriptions are a prerequisite for the inference of excited-state geometry changes from computed potential energy displacements. The development of time-dependent density functional theory (TDDFT) has provided a means for the economical computation of transition dipole moments at a given geometry.<sup>29,30</sup> It is desirable therefore, to apply these methods in the determination of the excited-state properties. Thus, in this paper, we have combined the technique of wave packet propagation with molecular parameters and energies from density functional theory (DFT) and time-resolved resonance Raman experiments to simulate the triplet excited state spectra of bromanil. To our knowledge, this is the first attempt to model the intensities of the triplet excited state using a combination of experimentally and theoretically determined parameters.

The parent benzoquinone and its fluorinated and chlorinated analogues have been studied extensively for their applications in biology and chemistry as electron acceptors in photochemical reactions. Benzoquinone is a well-studied system, both theoretically<sup>24,31</sup> and experimentally.<sup>32</sup> We have been involved in systematically investigating the effects of various substitutions on the structure of benzoquinone in the excited state.<sup>24,26–28,33–36</sup> In fluoranil,<sup>34</sup> we have shown that

the structure of the triplet excited state is less delocalized than in triplet benzoquinone due to the presence of perfluoro effect. Two opposite effects play a role in determining properties of perhalo substituted benzoquinones: inductively  $\sigma$ -withdrawing nature and the  $\pi$ -donation of the lone pairs of halogens.<sup>37</sup> Subtle changes in the structure due to substitution are known to alter the reactivity considerably in ketones. In bromanil, it is expected that the molecular properties would differ considerably from fluoranil, although both are halogen substitutions, since bromine is larger in size and less electron withdrawing than fluorine. Thus, we have taken the bromanil triplet excited state as an example to understand the mode-dependent shifts in the triplet state potential energy surfaces predicted by the simulation of the resonance Raman intensities.

## II. EXPERIMENTAL METHODS

Experimental methods and procedures used for the TR3 spectroscopy have been described previously.<sup>35</sup> Briefly, the pump beam is the third harmonic output of a 1064 nm fundamental from a Nd:YAG laser (DCR 11, Spectra Physics). The probe beam is obtained from an optical parametric oscillator (OPO) which is pumped by the third harmonic of 1064 nm output from an Nd:YAG laser (GCR 250, Spectra Physics). The probe wavelength 512 nm was obtained from the OPO. The pulses had typical energies of 2.5 mJ and were ca. 10 ns in temporal width for both pump and probe lasers. The scattered light was dispersed using a SPEX double monochromator with two 600 groves/mm gratings. The multichannel detector used was a liquid Nitrogen cooled CCD from Princeton Instruments with 576×378 pixels. The spectra have been calibrated using known solvent bands as reference, and the spectral resolution has been estimated as 5  $\text{cm}^{-1}$ . The concentration used for the Raman experiments was ca. 2 mM.

Bromanil used was purchased from Aldrich Chemicals. Both, bromanil and the solvents were of analytical grade and used without further purification. Sample solutions were circulated through a capillary at a rate of about 10 ml per minute to avoid possible accumulation of photoproducts. The probe only spectra were recorded periodically to confirm the absence of photoproducts.

## III. THEORY AND COMPUTATIONAL METHODS

Density functional theoretical calculations were performed with the Amsterdam Density Functional (ADF99) package<sup>38</sup> on a cluster of IBM RS 6000/43P workstations. Calculations for the triplet excited state used the unrestricted formalism. The basis set used was TZP (Basis IV in ADF terminology) that is a part of the ADF program.<sup>38</sup> The singlet-triplet excitation energies and the transition dipole lengths were computed using TDDFT as implemented in the Response<sup>29</sup> code in the ADF package of programs. Density functional calculations involved the local density approximation of Vosko, Wilk and Nussair (VWN),<sup>39</sup> gradient-corrected exchange functional proposed by Becke<sup>40</sup> and the correlation functional of Lee, Yang and Parr.<sup>41</sup> Normal mode analysis was carried out using NMODES,<sup>24</sup> a program devel-

oped in our laboratory which used the normal mode eigenvectors computed using the ADF package to compute the potential energy distribution. Wave packet dynamical simulations were carried out using MATLAB on an IBM RS 6000 workstation, using the analytical solutions mentioned below. The Fourier transform and inverse Fourier transform routines used were a part of the MATLAB library. Time step used for the simulation was 0.01 fs.

Lee and Heller's<sup>5</sup> time-dependent approach to resonance Raman scattering has been used to simulate the observed absorption and the relative Raman intensities. This time-domain picture of RR scattering has an intuitive appeal due to the simple physical picture that it provides for an understanding of the RR process. In this approach, the energy denominator of the sum-over-states expression of the Raman polarizability in Eq. (1)

$$\alpha_{if}(E_L) = M^2 \sum_{\nu} \frac{\langle f|\nu\rangle\langle\nu|i\rangle}{\epsilon_{\nu} - \epsilon_i + E_0 - E_L - i\Gamma} \quad (1)$$

is written in the form of an integral over a time variable.<sup>5</sup> If all the PES's are assumed to be harmonic and separable, we obtain the following expression for the Raman cross section in the time-domain,<sup>5,42</sup>

$$\sigma_{i \rightarrow f}(E_L) = \frac{8\pi E_L^3 E_s^4 M^4}{9\hbar^6 c^4} \left| \int_0^{\infty} \langle f|i(t)\rangle \times \exp\left[i(E_L + E_i)t/\hbar - \frac{\Gamma t}{\hbar} - \frac{\theta^2 t^2}{2\hbar}\right] dt \right|^2, \quad (2)$$

and the corresponding expression for the absorption spectrum is given by,

$$\sigma_A(E_L) = \frac{4\pi e^2 M^2 E_L}{6\hbar^2 c} \int_{-\infty}^{\infty} \langle i|i(t)\rangle \exp\left[i(E_L + E_i)t/\hbar - \frac{\Gamma|t|}{\hbar} - \frac{\theta^2 t^2}{2\hbar}\right] dt. \quad (3)$$

Here,  $|i(t)\rangle$  denotes the wave packet evolving on the resonant excited-state surface (RES) at various intervals of time ( $t$ ), under the influence of excited state vibrational Hamiltonian,  $H_{ex}$  given by the following expression:

$$|i(t)\rangle = \exp\left(-\frac{iH_{ex}t}{\hbar}\right)|i\rangle, \quad (4)$$

where  $\exp(-iH_{ex}t/\hbar)$  is the time evolution operator. Further, we have also assumed that there is no change in the vibrational normal modes on excitation, i.e., Duschinski rotation is not taken into account. The incident and scattered photon energies are  $E_L$  and  $E_s$ ;  $E_i$  is the zero-point vibrational energy of the  $T_1$  state, and  $M$  is the electronic transition dipole length evaluated at the equilibrium geometry of the  $T_1$  state for the transition from the  $T_1$  state to the resonant excited state (RES,  $T_n$ ),  $e$  is the electronic charge and  $c$  is the velocity of light. Motion of the time-evolving wave packet on the excited state is damped by two terms,  $\exp(-\Gamma t/\hbar)$  and  $\exp(-\theta^2 t^2/2\hbar)$ , which include broadening due to finite life-time ( $\Gamma$ ) as well as that induced by solvent ( $\theta$ ).

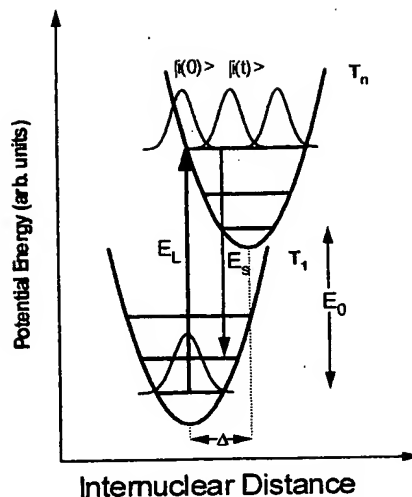


FIG. 1. Schematic representation of the physical picture provided by the time-dependent theory of resonance Raman intensities.

The physical interpretation provided by these equations is that the system is initially in a state  $|i\rangle$ , a vibrational eigen state of the lower triplet state ( $T_1$ ) surface. As shown in Fig. 1, the wave packet is transported to the  $T_n$  state via interaction of the transition dipole moment  $eM$ , of the  $T_1 \rightarrow T_n$  transition with the incident radiation of energy  $E_L$ . The vibrational state  $|i\rangle$  is not a stationary state of the  $T_n$  state and starts evolving under the influence of the excited state Hamiltonian,  $H_{ex}$  and is denoted by  $|i(t)\rangle$ . The absorption and Raman cross sections are obtained by taking the overlap of this time-evolving wave function with the ground vibrational state of the  $T_1$  state,  $|0\rangle$  (for absorption) and the first excited vibrational state of  $T_1$   $|1\rangle$  (for Raman).

The approximations stated earlier of harmonicity, separability, and equal frequencies lead to simplified expressions for the absorption and Raman cross sections<sup>15</sup> given by,

$$\sigma_A(E_L) = \frac{4\pi e^2 M^2}{6\hbar^2 c} \int_{-\infty}^{\infty} \exp\left[i(E_L - E_0)t/\hbar - \Gamma|t|/\hbar - \frac{\theta^2 t^2}{2\hbar}\right] \prod_{j=1}^N \exp\left[-\frac{\Delta_j^2}{2} [1 - \exp(-i\omega_j t)]\right] dt, \quad (5)$$

and

$$\sigma_{0 \rightarrow 1}(E_L) = \frac{8\pi e^4 M^4 E_s^3 E_L}{9\hbar^6 c^4} \left| \int_0^{\infty} \exp\left[i(E_L - E_0)t/\hbar - \Gamma|t|/\hbar - \frac{\theta^2 t^2}{2\hbar}\right] \frac{\Delta_1}{\sqrt{2}} (e^{-i\omega_1 t} - 1) \times \prod_{j=1}^N \exp\left[-\frac{\Delta_j^2}{2} [1 - \exp(-i\omega_j t)]\right] dt \right|^2, \quad (6)$$

where,  $E_0$  is the separation between the zero-point energies of the  $T_1$  and  $T_n$  states and  $\Delta_j$  denotes the relative dimensionless displacements between the PES's of the  $T_1$  and  $T_n$



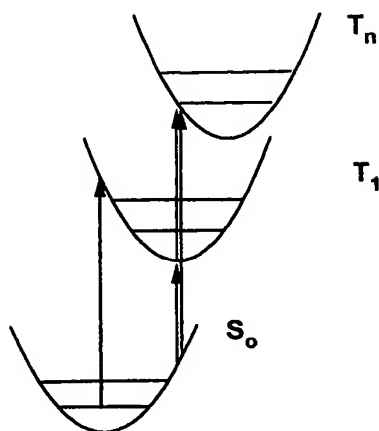


FIG. 2. Schematic representation of the energy differences in the singlet and triplet manifolds computed using TDDFT and DFT methods.

states along the  $j$ th mode. Therefore the parameters required for the simulation of the resonance Raman spectrum are the zero-zero energy ( $E_0$ ), the transition dipole length for the  $T_1 \rightarrow T_n$  transition, guess values for the displacements ( $\Delta_j$ ) and vibrational frequencies ( $\omega_j$ ) of the observed normal modes. In the following, we discuss each of these parameters along with the procedures used to obtain initial guesses in detail.

Initially, a DFT calculation was carried out to obtain the optimized geometry of the ground state ( $S_0$ ) of bromanil. Vibrational frequencies were computed and it was confirmed that the geometry is a minimum. Singlet-singlet and singlet-triplet excitations of bromanil were computed at this geometry using TDDFT. A comparison of the computed and experimentally reported  $S_0-T_1$  gap was made to identify the lowest triplet excited state. The geometry was optimized for the  $T_1$  state and vibrational frequencies were computed.

Subsequently, excitation energies are computed at the optimized triplet state geometry in order to identify the resonant triplet state by comparison with the observed maximum in the  $T_1 \rightarrow T_n$  transient absorption spectrum and predicted excitation energies illustrated schematically in Fig. 2. This is defined as the difference in energies:

$$\Delta E(T_1 \rightarrow T_n) = E(S_{\text{trip geom}} \rightarrow T_1) - E(S_{\text{trip geom}} \rightarrow T_n). \quad (7)$$

In principle, the transition dipole moment is a function of the nuclear coordinates,  $Q$ , because the Born-Oppenheimer electronic states depend parametrically on the nuclear coordinates. This coordinate dependence is neglected when on resonance with a strongly allowed transition (Condon approximation), i.e.,  $M(Q)$  is replaced with  $M(Q_0)$ , where  $Q_0$  is the fixed  $T_1$  state geometry. The transition dipole moment for the  $T_1 \rightarrow T_n$  transition therefore is computed at the equilibrium geometry of the  $T_1$  state.

In general, TDDFT only provides the transition dipole moment between the ground and excited states. Hence, the computation of the transition dipole moment between two excited (triplet) states used here requires some explanation. However, the formalism of TDDFT is very similar to the

singly excited CI calculation. If we assume that the Kohn-Sham single determinant is a reasonable, approximate description of the excited states in terms of a linear combination of determinants, singly excited with respect to the ground state. If we make this approximation, the transition dipole moments between these excited states are easily calculated.<sup>43</sup>

The separation of the  $T_1$  and the  $T_n$  states,  $E_0$ , determines the position of the absorption band. An initial guess is obtained from the computed excitation energy using TDDFT. The energy computed from the TDDFT calculation corresponds to the Franck-Condon excitation energy. The zero-zero separation is expected to be smaller than this value, in principle equal to the  $\Delta$ SCF energy, i.e., difference in the minimized energies of the  $T_1$  and  $T_n$  states. The guess displacements for the simulation are calculated from the ratios of relative intensities of the observed Raman spectra using the approximation  $I_j \propto \Delta_j^2 \omega_j^2$ .<sup>44</sup>

Finally, the broadening parameters affect the shape of the absorption spectrum but do not change the integrated absorption intensity. Fitting of the absorption spectrum alone, without the simultaneous modeling of the Raman excitation profile, can determine the total line width. However, relative magnitudes of homogeneous ( $\Gamma$ ) and inhomogeneous ( $\Theta$ ) broadening values computed from these simulations cannot be considered unique since the absorption spectrum is not sensitive to the partitioning of the homogeneous and inhomogeneous components.<sup>15,16</sup>

#### IV. RESULTS AND DISCUSSION

In a previous paper, we have reported the time-resolved resonance Raman spectra and assignments of the triplet excited state of bromanil in carbon tetrachloride.<sup>28</sup> The triplet state was populated via the singlet excited state by intersystem crossing by exciting with a pump laser at 355 nm. The probe laser at 512 nm, close to the maximum of the triplet-triplet absorption band (515 nm) was used to obtain the Raman spectrum. Four bands were observed at 1561, 1396, 1178, and 961  $\text{cm}^{-1}$  in the Raman spectrum shown in Fig. 3. The bands at 1561, 1396, and 961  $\text{cm}^{-1}$ , were assigned to fundamentals of  $a_g$  symmetry.<sup>28</sup> The assignments, computed spectra and potential energy distribution for the observed totally symmetric modes are summarized in Table I. The band at 1178  $\text{cm}^{-1}$  was assigned<sup>28</sup> to either a fundamental or overtone of a nontotally symmetric mode due to vibronic coupling of this mode with the nearby excited state,  $^3B_{1g}$ .

Since the objective of this paper is to compute the resonance Raman intensities and therefore the mode-dependent displacements of the PES of the excited state, we have modeled only these totally symmetric modes in the following intensity analyses. The measured depolarization ratios of all the totally symmetric bands are close to 0.3,<sup>28</sup> an indication that the intensities are derived from a single resonant state. It has been shown earlier by Tannor and Heller<sup>42</sup> that the wave packet dynamics in the harmonic case is separable into subspaces comprised of normal modes belonging to the same irreducible representation. The motion of the center of the wave packet is restricted to the totally symmetric subspace.



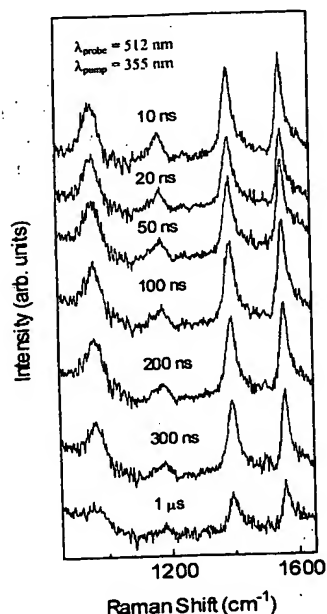


FIG. 3. Time-resolved resonance Raman spectra of triplet bromanil in carbon tetrachloride at various time delays between the pump and probe.

Only the totally symmetric bands are expected to be enhanced in a resonance Raman experiment and to have displacements in the excited state. The effect of the nontotally symmetric modes is only to broaden the spectrum.<sup>42</sup>

The optimized geometries and vibrational frequencies of the ground and triplet excited state of bromanil have been discussed in detail elsewhere.<sup>28</sup> Briefly, the triplet state was found to be of a lower symmetry ( $C_{2h}$ ) than the ground state ( $D_{2h}$ ). The effect of electronic excitation to the triplet state was found to be the largest along the C=O bond followed by the C=C bond. The C-C bond lengths were shortened on excitation. Both the high frequency modes at 1561 and 1395  $\text{cm}^{-1}$  were predicted to be coupled modes with different relative contributions of C=O and C=C stretching.

Table II lists the predicted singlet-triplet excitations computed at the optimized ground state geometry by TDDFT. The lowest  $S_0-T_n$  gap corresponds to the  $b_{1g} \rightarrow b_{2g}$  transition of 1.62 eV energy leading to a triplet state of  $B_{3g}$  symmetry. This is a  $\pi-\pi^*$  transition from the HOMO of  $b_{1g}$  symmetry of the ground state to the LUMO of  $b_{2g}$  symmetry. We note that there is another singlet-triplet excitation close to this from the HOMO-1 orbital of  $b_{3g}$  symmetry to the LUMO with excitation energy 1.74 eV of  $n-\pi^*$  character. Hence, TDDFT calculations predict relative ordering of the

TABLE I. Computed and experimental frequencies and potential energy distributions of the normal modes of triplet excited state of bromanil.

Sym.	PED%	Experimental	Calculated
$a_g$			
	C=C(35), C-C(27), C=O(20)	1561	1525
	C=O(60), C=C(37)	1395	1311
	C-Br(54), C-C(36)	965	901

TABLE II. Singlet-triplet excitation energies computed at the optimized ground state geometry ( $D_{2h}$ ) of bromanil by TDDFT calculations.

	State	Major MO's involved	Energy (eV)
1.	$^3B_{1g}$	$4b_{1g} \rightarrow 5b_{2g}$	1.62
2.	$^3B_{3g}$	$8b_{1g} \rightarrow 5b_{2g}$	1.74
3.	$^3B_{3u}$	$5b_{1u} \rightarrow 5b_{2g}$	2.13
4.	$^3A_u$	$9b_{2u} \rightarrow 5b_{2g}$	2.23
5.	$^3B_{1u}$	$9b_{3u} \rightarrow 5b_{2g}$	2.35
6.	$^3B_{3g}$	$7b_{1g} \rightarrow 5b_{2g}$	2.53
7.	$^3A_u$	$8b_{2u} \rightarrow 5b_{2g}$	2.90
8.	$^3A_g$	$4b_{2g} \rightarrow 5b_{2g}$	2.96
9.	$^3B_{2g}$	$10a_g \rightarrow 5b_{2g}$	3.12
10.	$^3B_{2u}$	$3a_u \rightarrow 5b_{2g}$	3.14

$\pi-\pi^*$  and  $n-\pi^*$  states in agreement with the experimental data of Schleglova and co-workers<sup>37</sup> where they have reported that the lowest triplet state in bromanil is the  $\pi-\pi^*$  state from their luminescence experiments.

Table III lists the singlet-triplet excitations computed at the triplet state geometry. As expected, the  $S_0-T_1$  gap is reduced to 1.20 eV and corresponds to the transition  $12b_g \rightarrow 15a_g$  in  $C_{2h}$  symmetry. The experimental absorption spectrum shown in Fig. 3 has a maximum at 2.41 eV. Therefore, the resonant excited state is expected at a singlet-triplet gap of 3.61 eV (1.20 eV + 2.41 eV). The transition with the energy closest to the maximum of the observed absorption spectrum (within the symmetry-allowed transitions) is identified as the  $12b_g \rightarrow 13a_u$  (81%) corresponding to the state,  $^3B_u$  with excitation energy 3.74 eV. The occupations of the unpaired electrons of the RES are:  $12b_g(1)13a_u(1)$ , leading to a final triplet state of  $B_u$  symmetry. Hence, the observed absorption spectrum is a transition from  $^3B_g \rightarrow ^3B_u$ , where the unpaired electron from the  $15a_g$  orbital is excited to the  $13a_u$  orbital. The transition dipole length computed from TDDFT is  $\langle 15a_g | \vec{\mu} | 13a_u \rangle = 0.97 \text{ \AA}$ . This computed value has been kept constant during the simulation. The  $T_1-T_n$  energy predicted by TDDFT, 2.51 eV (20 245  $\text{cm}^{-1}$ ) was used as the initial value of  $E_0$ .

Figure 4 shows the final simulated absorption spectrum (solid line) and Fig. 5 shows the excitation profiles for the three modes. The best-fit parameters obtained are  $E_0 = 16915 \text{ cm}^{-1}$ ,  $M = 0.97 \text{ \AA}$ ,  $\Gamma = 450 \text{ cm}^{-1}$  and  $\Theta$

TABLE III. Singlet-triplet excitation energies computed at the optimized triplet excited state geometry ( $C_{2h}$ ) using TDDFT calculations.

	State	Major MO's involved	Energy (eV)
1.	$^3B_g$	$12b_g \rightarrow 15a_g$	1.20
2.	$^3A_u$	$12a_u \rightarrow 15a_g$	1.70
3.	$^3B_u$	$14b_u \rightarrow 15a_g$	1.78
4.	$^3B_u$	$13b_u \rightarrow 15a_g$	1.98
5.	$^3A_u$	$11a_u \rightarrow 15a_g$	2.56
6.	$^3A_u$	$10a_u \rightarrow 15a_g$	2.80
7.	$^3B_u$	$12b_u \rightarrow 15a_g$	3.22
8.	$^3B_u$	$12b_g \rightarrow 13a_u$ (81%) $11b_g \rightarrow 13a_u$ (16%)	3.74
9.	$^3A_u$	$12a_u \rightarrow 16a_g$	4.45

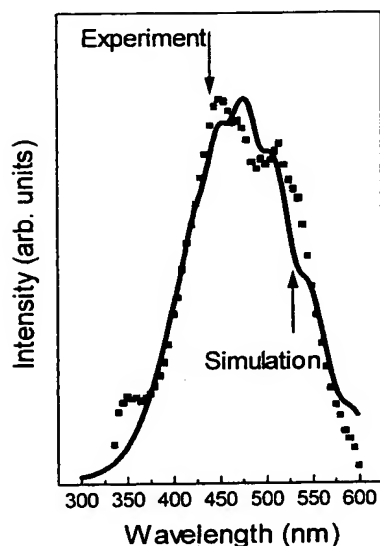


FIG. 4. Experimental (squares) and simulated (solid line) absorption spectra of triplet bromanil in carbon tetrachloride.

$= 150 \text{ cm}^{-1}$ . The corresponding mode-specific dimensionless displacements have been given in Table IV and the simulated spectrum has been shown in Fig. 6. The PES displacements obtained are similar for all three modes with 1.51 for the highest frequency mode at  $1561 \text{ cm}^{-1}$ , 1.61 and 1.53 for the modes at  $1396 \text{ cm}^{-1}$  and  $965 \text{ cm}^{-1}$ , respectively. As shown in Fig. 7, the mode at  $1561 \text{ cm}^{-1}$  has contributions from the C=C str. C=O str. and the C-C str. Similarly for the mode at  $1396 \text{ cm}^{-1}$ , both the C=O and C=C str. are involved. We note that the sign of the displacement is not determined by

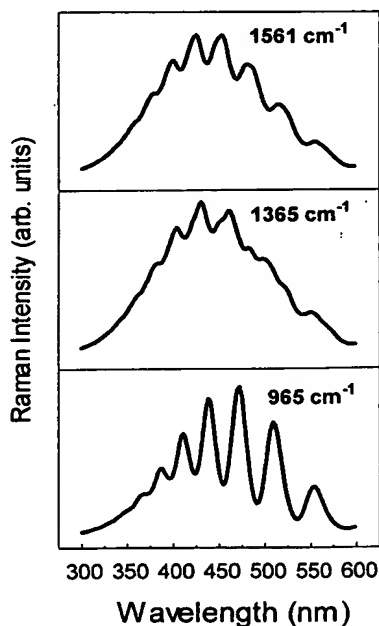


FIG. 5. Simulated Raman excitation profiles for each of the observed fundamental modes.

TABLE IV. Best-fit values of the dimensionless displacements obtained from the simulation with  $E_0 = 16\,915 \text{ cm}^{-1}$ ,  $\Gamma = 450 \text{ cm}^{-1}$ ,  $\Theta = 150 \text{ cm}^{-1}$ .

Frequency ( $\omega_i \text{ cm}^{-1}$ )	Displacement ( $\Delta_i$ )	Relative intensities	
		Experimental	Calculated
1561	1.51	1.0	1.0
1396	1.61	0.87	0.88
965	1.53	0.58	0.56

these simulations, since only the square of the displacement appears in the analytical expressions of the cross sections. Therefore, interpretation of the computed displacements, in terms of the changes in bond lengths, has been carried out by using the knowledge of the nature of the ground state MO involved in the formation of the  $T_n$  state.

The similar displacements in all the modes indicate that the changes in structure in RES with respect to the  $T_1$  state are not localized to a specific part of the molecule but are spread over the entire molecule. This may be rationalized from the nature of the ground state molecular orbitals involved in these states as follows. The  $T_1$  state involves population of the LUMO, which is delocalized over the carbonyl groups and the C-C bonds. It was shown earlier<sup>28</sup> that the geometry of the  $T_1$  state could be explained from the nodal structure of the LUMO of the ground state. The LUMO has bonding interaction with the C-C-C atoms and antibonding interaction between the carbon and oxygen of the carbonyl group. As a consequence, in the  $T_1$  state, the C-C bonds were shortened and the C=O bonds were lengthened in comparison with the ground state. The  $T_n$  state is formed by removing the electron from the LUMO and populating the higher unoccupied MO( $13a_u$ ) which is shown in Fig. 8. The orbital has antibonding character between the carbon atoms of the C=C bond. Therefore, qualitatively, the expected

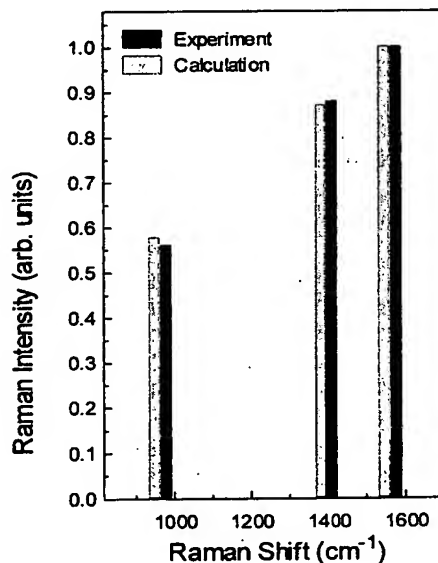


FIG. 6. Experimental and simulated resonance Raman intensities of bromanil.

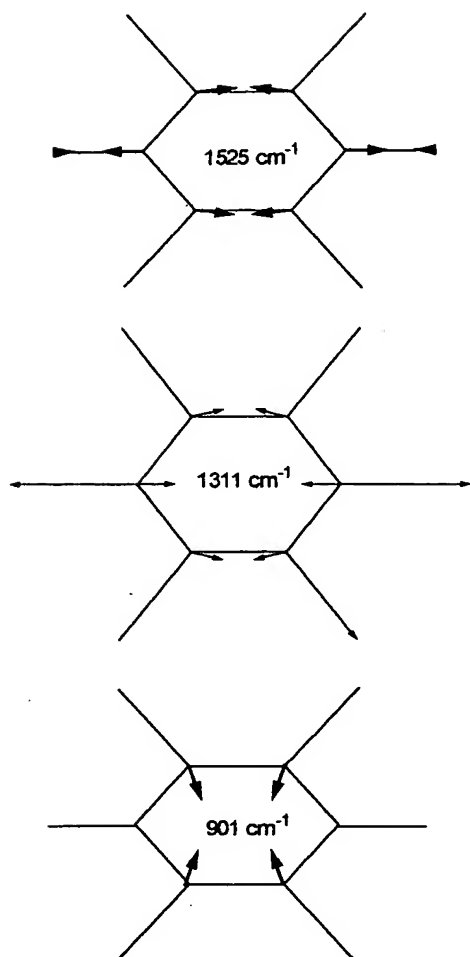


FIG. 7. Normal mode displacements of triplet bromanil for the observed modes.

changes in the geometry of bromanil in the  $T_n$  state as compared to the  $T_1$  state are: (1) The C=O bond length should decrease due to removal of the electron from the C=O antibonding LUMO, (2) the C-C bond length should increase, and (3) the C=C bond should be longer due to antibonding nature of the  $a_u$  orbital. The computed displacements bear out the expected geometrical changes.

Table V lists the optimized geometry in the  $T_n$  state identified from comparison of the experimental absorption and TDDFT calculations. Previously reported geometries of the ground state and  $T_1$  state are also given for comparison. In the  $T_n$  state, the C=C and C-C bond lengths are increased to 1.389 Å and 1.480 Å. The C=O bond length decreases to 1.215 Å. The trends in the geometries predicted using DFT are in agreement with those predicted by the simulated displacements. The difference in the bonding energies ( $\Delta E_{\text{SCF}}$ ) of the  $T_1$  and the  $T_n$  states is found to be 16739  $\text{cm}^{-1}$ . The best-fit value of  $E_0$  obtained from the simulations was 16915  $\text{cm}^{-1}$ , close to the SCF energy difference. The difference between the computed Franck-Condon excitation energy (TDDFT) and zero-zero separation

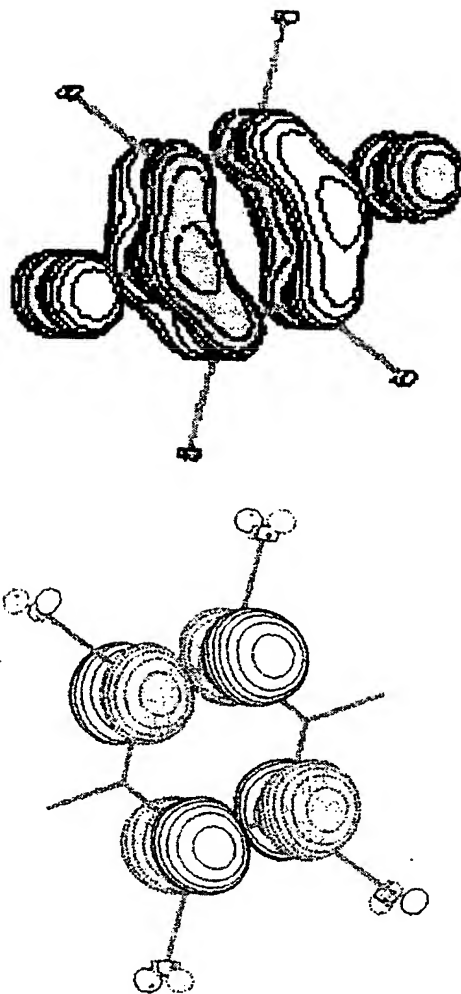


FIG. 8. Computed molecular orbitals of bromanil in the ground state LUMO and the  $13a_u$  orbital.

( $\Delta E_{\text{SCF}}$ ) and that obtained from experiments ( $\lambda_{\text{max}}$ ) and simulations ( $E_0$ ) are close to each other.

## V. SUMMARY

The theory of resonance Raman intensities has been applied to the triplet excited state using the techniques of wave packet dynamics and density functional theory. The simula-

TABLE V. Calculated geometries of the ground and lowest triplet excited states and the resonant triplet state of bromanil.

	Ground state ( $D_{2h}$ )	Lowest triplet state $T_1(C_{2h})$	Excited triplet state $T_n(C_{2h})$
$R(\text{C}=\text{C})$	1.341	1.369	1.389
$R(\text{C}=\text{O})$	1.212	1.251	1.215
$R(\text{C}-\text{C})$	1.485	1.440	1.480
$R(\text{C}-\text{Br})$	1.883	1.885	1.889
$\alpha(\text{C}=\text{C}-\text{C})$	121.6	122.2	121.5
$\alpha(\text{C}-\text{C}-\text{C})$	116.9	115.6	116.7
$\alpha(\text{C}=\text{C}-\text{Br})$	123.5	122.8	122.3

tions yield valuable information on the structure and PES of the resonant higher triplet state. The observed  $T_1 \rightarrow T_n$  absorption spectrum is assigned to the  ${}^3B_g \rightarrow {}^3B_u$  transition. The geometry has been optimized for the resonant higher triplet state,  $T_n$ , and is found to be in good agreement with the predictions of the wave packet dynamical simulations. The triplet-triplet energy separation predicted by TDDFT is close to the separation obtained from the  $\lambda_{\max}$  of the transient absorption experiment (Franck-Condon excitation energy) and the zero-zero energy separation obtained from DFT ( $\Delta$ SCF) is close to the best-fit value obtained from the simulations.

Thus, it has been demonstrated that TR3 spectra can be simulated to obtain valuable structural and dynamical information like the energy separation between the lowest triplet state and the resonant excited-state ( $T_n$ ), nature of the  $T_n$  and its PES and initial mode-specific dynamics of the reactive triplet state. However, it is important to appreciate the caveats in such an approach. It is well known that accurate measurement of resonance Raman intensities is difficult. While the transient state excitation profiles would in principle yield more information, they are prone to several possible sources of error, which must be carefully accounted for. The simple analytical solutions used here assume only one resonant excited state. Therefore, these cannot be applied to molecules where the transient state resonance Raman spectra indicate the presence of multiple electronic states.

The dimensionless displacement parameters obtained from these simulations are relative values and the sign of the displacement is not known. Combined information from simulations and DFT enables interpretation of the computed displacements to physically meaningful changes in geometry. Thus, it is possible to extract valuable information on the mode-specific dynamics in the triplet excited state, which is a precursor to several photochemical reactions.

## ACKNOWLEDGMENTS

The authors thank the Department of Science and Technology (DST) and the Council of Scientific and Industrial Research (CSIR), Government of India, for financial support. One of the authors (M.P.) thanks Unilever India Inc., NUFIC, and Dutch Ministry for Culture, Education and Science, The Netherlands, for a visiting fellowship.

- <sup>1</sup>R. E. Hester, in *Advances in Infrared and Raman Spectroscopy*, edited by R. J. H. Clark and R. E. Hester (Heyden, London, 1978), Vol. 4, p. 1.
- <sup>2</sup>G. H. Atkinson, in *Advances in Infrared and Raman Spectroscopy*, edited by R. J. H. Clark and R. E. Hester (Heyden, London, 1982), Vol. 9, p. 1.
- <sup>3</sup>H. Hamaguchi, in *Vibrational Spectra and Structure*, edited by J. R. Durig (Elsevier, Amsterdam, 1987), Vol. 16, p. 227.
- <sup>4</sup>G. N. R. Tripathi, in *Time Resolved Spectroscopy*, edited by R. J. H. Clark and R. E. Hester (John Wiley and Sons, Ltd., London, 1989), Vol. 18, Chapter 4, p. 157.
- <sup>5</sup>S. Lee and E. J. Heller, *J. Chem. Phys.* **71**, 4777 (1979).
- <sup>6</sup>R. Mathies, in *Chemical and Biochemical Applications of Lasers*, edited by C. B. Moore (Academic, New York, 1979), Vol. 4, p. 55.
- <sup>7</sup>A. B. Myers and R. A. Mathies, *J. Chem. Phys.* **81**, 1552 (1984).
- <sup>8</sup>J. Rodier and A. B. Myers, *J. Am. Chem. Soc.* **115**, 10791 (1993).
- <sup>9</sup>N. Biswas and S. Umapathy, *J. Chem. Phys.* **107**, 7849 (1997).
- <sup>10</sup>N. Biswas and S. Umapathy, *Chem. Phys. Lett.* **236**, 24 (1995).
- <sup>11</sup>N. Biswas and S. Umapathy, *Chem. Phys. Lett.* **294**, 181 (1998).

- <sup>12</sup>A. P. Esposito, C. E. Foster, R. A. Beckman, and P. J. Reid, *J. Phys. Chem. A* **101**, 5309 (1997).
- <sup>13</sup>L. M. Markham and B. S. Hudson, *J. Phys. Chem.* **100**, 2731 (1996).
- <sup>14</sup>E. J. Heller, *Acc. Chem. Res.* **14**, 368 (1981).
- <sup>15</sup>A. B. Myers and R. A. Mathies, in *Biochemical Applications of Raman Spectroscopy*, edited by T. G. Spiro (Wiley, New York, 1987), Vol. 2, p. 1.
- <sup>16</sup>A. B. Myers, *J. Raman Spectrosc.* **28**, 389 (1997); A. B. Myers, *Chem. Rev.* **96**, 911 (1996); A. B. Myers, in *Laser Techniques in Chemistry*, Techniques of Chemistry Series, Vol. 23, edited by A. B. Myers and T. R. Rizzo (Wiley and Sons Inc., New York, 1995), pp. 325-384.
- <sup>17</sup>J. L. Zink and K.-S. K. Shin, *Adv. Photochem.* **16**, 119 (1991).
- <sup>18</sup>N. Biswas and S. Umapathy, *Curr. Sci.* **74**, 328 (1998).
- <sup>19</sup>L. M. Markham, L. C. Mayne, B. S. Hudson, and M. Z. Zgierski, *J. Phys. Chem.* **97**, 10319 (1993); B. S. Hudson and L. M. Markham, *J. Raman Spectrosc.* **29**, 489 (1998).
- <sup>20</sup>T. Keszthelyi, G. Balakrishnan, R. Wilbrandt, W. A. Yee and F. Negri, *J. Phys. Chem. A* **104**, 9121 (2000); A. M. Brouwer, J. M. Zwier, C. Svendsen, O. S. Mortensen, F. W. Langkilde, and R. Wilbrandt, *J. Am. Chem. Soc.* **120**, 3748 (1998); A. M. Brouwer, C. Svendsen, O. S. Mortensen, and R. Wilbrandt, *J. Raman Spectrosc.* **29**, 439 (1998).
- <sup>21</sup>F. W. Langkilde, R. Wilbrandt, A. M. Brouwer, F. Negri, and G. Orlandi, *J. Phys. Chem.* **98**, 2254 (1994); F. W. Langkilde, R. Wilbrandt, S. Moller, A. M. Brouwer, F. Negri, and G. Orlandi, *J. Phys. Chem.* **95**, 6884 (1991); F. Negri, G. Orlandi, A. M. Brouwer, F. W. Langkilde, S. Moller, and R. Wilbrandt, *J. Phys. Chem.* **95**, 6895 (1991); F. Negri, G. Orlandi, A. M. Brouwer, F. W. Langkilde, and R. Wilbrandt, *J. Chem. Phys.* **90**, 5944 (1989).
- <sup>22</sup>S. E. Boesch and R. A. Wheeler, *J. Phys. Chem.* **99**, 8125 (1995); S. E. Boesch and R. A. Wheeler, *J. Phys. Chem.* **101**, 8351 (1997).
- <sup>23</sup>D. Pan, L. C. T. Shoute, and D. L. Phillips, *J. Phys. Chem. A* **103**, 6851 (1999); D. Pan, L. C. T. Shoute, and D. L. Phillips, *J. Phys. Chem. A* **104**, 4140 (2000).
- <sup>24</sup>P. Mohandas and S. Umapathy, *J. Phys. Chem. A* **101**, 4449 (1997).
- <sup>25</sup>N. Biswas and S. Umapathy, *J. Phys. Chem.* **101**, 5555 (1997); N. Biswas and S. Umapathy, *J. Phys. Chem.* **104**, 2734 (2000).
- <sup>26</sup>G. Balakrishnan, P. Mohandas, and S. Umapathy, *Spectrochim. Acta, Part A* **53**, 153 (1997).
- <sup>27</sup>G. Balakrishnan, P. Mohandas, and S. Umapathy, *J. Phys. Chem. A* (in press).
- <sup>28</sup>M. Puranik, J. Chandrasekhar, J. G. Snijders, and S. Umapathy, *J. Phys. Chem.* (unpublished).
- <sup>29</sup>S. J. A. van Gisbergen, J. G. Snijders, and E. J. Baerends, *Comput. Phys. Commun.* **118**, 119 (1999).
- <sup>30</sup>A. Rosa, E. J. Baerends, S. J. A. van Gisbergen, E. van Lenthe, and J. G. Snijders, *J. Am. Chem. Soc.* **121**, 10356 (1999); S. J. A. van Gisbergen, J. A. Groeneveld, A. Rosa, J. G. Snijders, and E. J. Baerends, *J. Phys. Chem. A* **103**, 6835 (1999); S. J. A. van Gisbergen, J. G. Snijders, and E. J. Baerends, *Phys. Rev. Lett.* **78**, 3097 (1997).
- <sup>31</sup>D. M. Chipman and M. F. Prebenda, *J. Phys. Chem.* **90**, 5557 (1986).
- <sup>32</sup>R. Rossetti and L. E. Brus, *J. Am. Chem. Soc.* **108**, 4718 (1986); S. M. Beck and L. E. Brus, *J. Am. Chem. Soc.* **104**, 4789 (1982); R. H. Schuler, G. N. R. Tripathi, M. F. Prebenda, and D. M. Chipman, *J. Phys. Chem.* **87**, 3101 (1983).
- <sup>33</sup>G. Balakrishnan, A. Babaei, A. J. McQuillan, and S. Umapathy, *J. Biomol. Struct. Dyn.* **16**, 123 (1998); G. Balakrishnan and S. Umapathy, *J. Mol. Struct.* **475**, 5 (1999).
- <sup>34</sup>G. Balakrishnan and S. Umapathy, *Chem. Phys. Lett.* **270**, 557 (1997); G. Balakrishnan and S. Umapathy, *J. Chem. Soc., Faraday Trans.* **93**, 4125 (1997); M. Puranik, H. Mohapatra, G. Balakrishnan, J. Chandrasekhar, and S. Umapathy, *Asian J. Phys.* **2**, 189 (1998).
- <sup>35</sup>G. Balakrishnan, P. Mohandas, and S. Umapathy, *J. Phys. Chem.* **100**, 16472 (1996).
- <sup>36</sup>M. Puranik, J. Chandrasekhar, and S. Umapathy, *Chem. Phys. Lett.* **337**, 224 (2001).
- <sup>37</sup>N. A. Shcheglova, D. N. Shigorin, G. G. Yakobson, and L. Sh. Tushishvili, *Russ. J. Phys. Chem.* **43**, 1112 (1969).
- <sup>38</sup>(a) ADF 1999, E. J. Baerends, A. Bércecs, C. Bo *et al.*; (b) E. J. Baerends, D. E. Ellis, and P. Ros, *Chem. Phys.* **2**, 41 (1973); (c) L. Versluis and T. Ziegler, *J. Chem. Phys.* **322**, 88 (1988); (d) G. te Velde and E. J. Baerends, *J. Comput. Phys.* **99**, 84 (1992); (e) C. F. Guerra, J. G. Snijders, G. te Velde, and E. J. Baerends, *Theor. Chem. Acc.* **99**, 391 (1998).

**This Page is Inserted by IFW Indexing and Scanning  
Operations and is not part of the Official Record**

**BEST AVAILABLE IMAGES**

Defective images within this document are accurate representations of the original documents submitted by the applicant.

Defects in the images include but are not limited to the items checked:

- ☐ BLACK BORDERS
- ☐ IMAGE CUT OFF AT TOP, BOTTOM OR SIDES
- ☐ FADED TEXT OR DRAWING
- ☐ BLURRED OR ILLEGIBLE TEXT OR DRAWING
- ☐ SKEWED/SLANTED IMAGES
- ☐ COLOR OR BLACK AND WHITE PHOTOGRAPHS
- ☐ GRAY SCALE DOCUMENTS
- ☐ LINES OR MARKS ON ORIGINAL DOCUMENT
- ☒ REFERENCE(S) OR EXHIBIT(S) SUBMITTED ARE POOR QUALITY
- ☐ OTHER: \_\_\_\_\_

**IMAGES ARE BEST AVAILABLE COPY.**

**As rescanning these documents will not correct the image problems checked, please do not report these problems to the IFW Image Problem Mailbox.**